

# A Semi-Implicit Variational Multiscale Formulation for the Incompressible Navier–Stokes Equations via Exact Adjoint Linearization

Biswajit Khara<sup>1\*</sup>, Suresh Murugaiyan<sup>1</sup>, Suriya Dhakshinamoorthy<sup>2</sup>, Makrand Khanwale<sup>3</sup>, Ming-Chen Hsu<sup>2</sup>, and Baskar Ganapathysubramanian<sup>1,2\*</sup>

<sup>1</sup>Translational AI Center, Iowa State University, Ames, IA

<sup>2</sup>Department of Mechanical Engineering, Iowa State University, Ames, IA

<sup>3</sup>Department of Mechanical Engineering, Stanford University, Stanford, CA

## Abstract

A semi-implicit, residual-based variational multiscale (VMS) formulation is developed for the incompressible Navier–Stokes equations. The approach linearizes convection using an extrapolated (Oseen-type) convecting velocity, producing a linear advection operator at each time step. For this operator, the adjoint can be written exactly. Exploiting this exact adjoint yields a systematic derivative-transfer mechanism within the VMS closure. In particular, unresolved-scale contributions enter the weak form without spatial derivatives of the modeled fine-scale velocity. The resulting terms also avoid derivatives of coarse-scale residuals and stabilization parameters. This eliminates the boundary-condition-sensitive, case-by-case integrations by parts that often accompany nonlinear residual-based VMS implementations, and it simplifies implementation in low-order FEM settings.

The formulation is presented for a generalized linear convection operator encompassing three common advection forms (convective-, skew-symmetric- and divergence-form). Their numerical behavior is compared, along with the corresponding fully implicit nonlinear VMS counterparts. Because the method is linear by construction, each time step requires only one linear solve. Across the benchmark suite, this reduces wall-clock time by 2–4× relative to fully implicit nonlinear formulations while maintaining comparable accuracy. Temporal convergence is verified, and validation is performed on standard problems including the lid-driven cavity, flow past a cylinder, turbulent channel flow, and turbulent flow over a NACA0012 airfoil at chord Reynolds number  $6 \times 10^6$ . Overall, the convective and the skew-symmetric forms remain robust across the test cases, whereas the divergence-form can become nonconvergent for problems with purely Dirichlet boundaries.

## 1 Introduction

In many important applications, the finite element method (FEM) is a method of choice for solving the incompressible Navier–Stokes equations (NSE), especially for multiphysics couplings (e.g., fluid–structure interaction) and flows on complex geometries. Yet, a direct application of standard Galerkin FEM to the incompressible NSE is well known to be problematic [1, 2]. Two distinct instabilities arise. First, because pressure does not appear in the continuity equation, the discrete problem is a saddle-point system; unless the velocity–pressure spaces satisfy an inf–sup condition, spurious pressure (and velocity) oscillations result [3, 4]. Second, in convection-dominated regimes, the standard Galerkin formulation lacks the necessary numerical dissipation and exhibits nonphysical oscillations [5]. These challenges have motivated a broad class of remedies, including nonconforming formulations [6, 7], inf–sup stable elements [8, 9], and residual-based stabilizations [10, 11, 12, 13].

In this work, we focus on the variational multiscale (VMS) framework [14, 15, 16, 17], which provides a unified stabilization mechanism for both the saddle-point structure and convection-driven instabilities. VMS decomposes the solution into *coarse scales* (resolved by the finite element space) and *fine scales* (unresolved by the mesh). The fine scales are not explicitly represented, but their effect on the resolved scales is incorporated through a closure model that expresses fine-scale dynamics in terms of coarse-scale residuals and stabilization

parameters. In classical residual-based VMS, this yields pressure stabilization and SUPG-like upwinding within a consistent variational setting.

However, when VMS is applied to nonlinear operators (such as the Navier-Stokes equations), it results in nonlinear coupling between the resolved and unresolved scales, and the resulting formulation yields terms involving spatial derivatives of the unresolved velocity  $u'$ . These derivatives depend on derivatives of the coarse-scale residual and on spatial variations of the stabilization parameters. In low-order FEM implementations, such terms are either ill-defined or require additional manipulations. The standard remedy is to “transfer” derivatives off  $u'$  via integration by parts and related identities. However, for nonlinear convection this transfer is typically performed in a case-by-case (and often boundary-condition-dependent) manner, leading to formulations that are less transparent and harder to reproduce or extend (see [Section 2](#)). This paper addresses this difficulty by developing a *semi-implicit* VMS formulation in which the convection operator is linearized (Oseen-type) using known information from previous time levels. Linearization has two coupled benefits. First, it yields a *derivative-free unresolved-scale representation*: by this we mean a weak formulation in which unresolved-scale contributions appear *without spatial derivatives of  $u'$*  (and hence without derivatives of residuals or stabilization parameters), so that all fine-scale terms can be expressed using coarse-scale residuals and the chosen test spaces only. This removes the need for additional weakening steps and the associated special treatment of boundary terms. Second, because the resulting scheme is linear at each time step, it requires the solution of *one linear system per time step*, offering substantial computational savings relative to fully implicit nonlinear VMS formulations.

The key technical observation underpinning the derivative-free representation is that when the convection operator is linear, its adjoint can be computed *exactly*. Within the VMS framework, this exact adjoint provides a systematic and reproducible mechanism for transferring derivatives from unresolved-scale terms to the test functions without requiring ad hoc manipulations. This yields a semi-implicit VMS method that is both implementation-friendly and methodologically transparent. Beyond implementation simplicity, avoiding derivatives of  $u'$  is also important for extensibility. Formulations that minimize boundary-condition-sensitive integration-by-parts arguments are easier to integrate with discretizations and geometric technologies that complicate boundary term bookkeeping, such as shifted boundary methods (SBM) and immersed/implicit geometry approaches (e.g., IMGA). In such settings, reducing special boundary treatments is particularly valuable.

Building on these ideas, our contributions are:

1. *Exact-adjoint observation and derivative-free unresolved-scale representation:* We show that once the convection operator is linearized, its adjoint can be computed *exactly*. Within a residual-based VMS closure, this enables a systematic transfer of derivatives from unresolved-scale terms onto the test functions, yielding a formulation in which the unresolved-scale contributions appear *without spatial derivatives of  $u'$*  (and hence without derivatives of residuals or stabilization parameters). This eliminates the need for ad hoc weakening steps and reduces sensitivity to boundary-condition-specific integration-by-parts manipulations.
2. *General semi-implicit VMS formulation and convection-form comparison:* Using the above mechanism, we derive a semi-implicit residual-based VMS formulation for the incompressible NSE based on a generalized linear convection operator, and we present and compare three common linear advection forms.
3. *Computational efficiency:* The proposed method is linear by construction and requires only a single linear solve per time step, providing a significant speedup compared to fully implicit nonlinear VMS formulations.
4. *Verification and validation:* We verify temporal convergence and validate the method on a suite of standard benchmark problems, comparing its accuracy and computational cost with those of fully implicit counterparts.

The remainder of this paper is organized as follows. In [Section 2](#), we review preliminaries and motivate the current work. In [Section 3](#), we present the semi-implicit VMS formulation for a general linear convection operator, and provide some implementation details in [Section 4](#). We report our numerical results in [Section 5](#), and conclude our discussions in [Section 6](#).

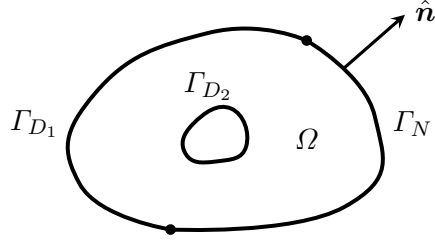


Figure 1: Sketch of a general domain with different conditions applied at different boundaries. Neumann conditions are prescribed on  $\Gamma_N$ , and Dirichlet conditions on the velocities are prescribed on  $\Gamma_{D_1}$  and  $\Gamma_{D_2}$ .

## 2 Preliminaries and motivation

In this section, we give a brief overview of the fully implicit VMS formulation, highlighting the important steps and illustrating the issues encountered. The presentation in this section also lays down the basic terminologies and sets the stage for the next section.

### 2.1 Notation

Throughout this paper, we will denote vector-valued quantities by boldface letters. For example,  $\mathbf{x}$  given by

$$\mathbf{x} = [x_1, x_2, \dots, x_d]^T = \begin{bmatrix} x_1 \\ x_2 \\ \vdots \\ x_d \end{bmatrix}$$

denotes the spatial coordinates where each  $x_i, i = 1, 2, \dots, d$  are scalars. Similarly,  $\mathbf{u}(t, \mathbf{x}) = [u_1, u_2, \dots, u_n]^T$  denotes a vector-valued *function* where each  $\{u_i\}_{i=1}^n$  is a function of both time and space, i.e.,  $u_i = u_i(t, \mathbf{x})$ .

Given two scalar-valued functions  $a(\mathbf{x})$  and  $b(\mathbf{x})$  on a domain  $\Omega \subset \mathbb{R}^d$ , we denote the inner-product between them as

$$(a, b) := \int_{\Omega} a(\mathbf{x}) b(\mathbf{x}) d\mathbf{x}.$$

For two *vector-valued* functions  $\mathbf{a}(\mathbf{x})$  and  $\mathbf{b}(\mathbf{x})$ , we denote the inner-product in a similar manner as

$$(\mathbf{a}, \mathbf{b}) := \int_{\Omega} \mathbf{a}(\mathbf{x}) \cdot \mathbf{b}(\mathbf{x}) d\mathbf{x} = \int_{\Omega} \mathbf{a}(\mathbf{x})^T \mathbf{b}(\mathbf{x}) d\mathbf{x} = \int_{\Omega} \left[ \sum_{i=1}^n a_i(\mathbf{x}) b_i(\mathbf{x}) \right] d\mathbf{x} = \sum_{i=1}^n (a_i, b_i).$$

### 2.2 Implicit Galerkin formulation of the Navier-Stokes equations

Suppose  $\Omega$  is a spatial domain (see Figure 1). The incompressible Navier-Stokes equations in non-dimensional form on  $\Omega$  are

$$\partial_t \mathbf{u} + (\mathbf{u} \cdot \nabla) \mathbf{u} + s(\nabla \cdot \mathbf{u}) \mathbf{u} - \nu \Delta \mathbf{u} + \nabla p - \mathbf{f} = \mathbf{0}, \quad (1a)$$

$$\nabla \cdot \mathbf{u} = 0, \quad (1b)$$

along with the boundary conditions

$$\mathbf{u} = \mathbf{u}_{D_1} \text{ on } \Gamma_{D_1}, \quad (2a)$$

$$\mathbf{u} = \mathbf{u}_{D_2} \text{ on } \Gamma_{D_2}, \quad (2b)$$

$$\hat{\mathbf{n}} \cdot (-p \mathbf{I} + \nu \nabla \mathbf{u}) = \mathbf{h} \text{ on } \Gamma_N, \quad (2c)$$

and initial conditions

$$\mathbf{u}(t = 0, \cdot) = \mathbf{u}_0(\cdot). \quad (3)$$

Here,  $\mathbf{u}$ ,  $p$  and  $\mathbf{f}$  are the velocity, pressure, and forcing, respectively. The parameter  $\nu$  is the dimensionless viscosity ( $\nu = Re^{-1}$ ). The scalar parameter  $s \in \{0, 1\}$  is introduced to toggle between two equivalent nonlinear convection representations,

$$(\mathbf{u} \cdot \nabla) \mathbf{u} + s(\nabla \cdot \mathbf{u}) \mathbf{u} = \begin{cases} (\mathbf{u} \cdot \nabla) \mathbf{u}, & \text{when } s = 0 \quad (\text{convective form}), \\ \nabla \cdot (\mathbf{u} \mathbf{u}^T), & \text{when } s = 1 \quad (\text{divergence form}), \end{cases} \quad (4)$$

using the identity  $\nabla \cdot (\mathbf{u} \mathbf{u}^T) = (\mathbf{u} \cdot \nabla) \mathbf{u} + (\nabla \cdot \mathbf{u}) \mathbf{u}$ . Although these forms are equivalent at the continuous level under  $\nabla \cdot \mathbf{u} = 0$ , they lead to different weak forms once modeling and stabilization are introduced. We retain this parameterization because the semi-implicit development in [Section 3](#) will treat a generalized *linear* convection operator in an analogous way.

Equations (1)–(3) form a system that can be solved numerically. For unique solvability, at least one Dirichlet condition on the velocity is required. We assume  $\Gamma_{D_1} \neq \emptyset$ , while  $\Gamma_{D_2}$  may be empty.

To solve (1) numerically, we prescribe temporal and spatial discretizations. We employ implicit time stepping (using backward difference formula (BDF) methods) and a continuous Galerkin finite element method in space. An  $r$ -th order BDF approximation of  $\partial \mathbf{u} / \partial t$  at time step  $n$  is

$$\frac{\partial \mathbf{u}}{\partial t} \Big|_n = \frac{1}{\Delta t} \sum_{i=0}^r \beta_{-i} \mathbf{u}^{n-i} = \sigma \mathbf{u}^n + \frac{1}{\Delta t} \sum_{i=1}^r \beta_{-i} \mathbf{u}^{n-i}, \quad (5)$$

where  $\sigma = \beta_0 / \Delta t$  and  $\{\beta_{-i}\}$  depend on  $r$ . In a time-marching setting,  $\mathbf{u}^n$  is unknown, while  $\mathbf{u}^{n-1}, \dots, \mathbf{u}^{n-r}$  are known. The BDF- $r$  discretization of (1) reads

$$\sigma \mathbf{u}^n + (\mathbf{u}^n \cdot \nabla) \mathbf{u}^n + s(\nabla \cdot \mathbf{u}^n) \mathbf{u}^n - \nu \Delta \mathbf{u}^n + \nabla p^n - \mathbf{g}^n = \mathbf{0}, \quad (6a)$$

$$\nabla \cdot \mathbf{u}^n = 0, \quad (6b)$$

where

$$\mathbf{g}^n := \mathbf{f}^n - \frac{1}{\Delta t} \sum_{i=1}^r \beta_{-i} \mathbf{u}^{n-i}. \quad (7)$$

We now derive a Galerkin formulation of (6). Define the trial and test spaces

$$\mathbf{V}^D := \{\mathbf{v} \in \mathbf{H}^1(U) : \mathbf{v} = \mathbf{u}_{D_1} \text{ on } \Gamma_{D_1}, \mathbf{v} = \mathbf{u}_{D_2} \text{ on } \Gamma_{D_2}\}, \quad (8a)$$

$$\mathbf{V} := \{\mathbf{v} \in \mathbf{H}^1(U) : \mathbf{v} = \mathbf{0} \text{ on } \Gamma_{D_1} \cup \Gamma_{D_2}\}, \quad (8b)$$

$$Q := H^1(U). \quad (8c)$$

We seek  $(\mathbf{u}^n, p^n) \in \mathbf{V}^D \times Q$  such that, for all  $(\mathbf{v}, q) \in \mathbf{V} \times Q$ ,

$$\int_{\Omega} \mathbf{v} \cdot [\sigma \mathbf{u}^n + (\mathbf{u}^n \cdot \nabla) \mathbf{u}^n + s(\nabla \cdot \mathbf{u}^n) \mathbf{u}^n - \nu \Delta \mathbf{u}^n + \nabla p^n - \mathbf{g}^n] \, d\mathbf{x} + \int_{\Omega} q \nabla \cdot \mathbf{u}^n \, d\mathbf{x} = 0. \quad (9)$$

We can perform integration-by-parts on the “stress” terms, i.e., the Laplacian  $\Delta \mathbf{u}^n$  and the pressure gradient  $\nabla p^n$  as follows.

$$\int_{\Omega} \mathbf{v} \cdot (-\nu \Delta \mathbf{u}^n) \, d\mathbf{x} = \int_{\Omega} \nu \nabla \mathbf{v} : \nabla \mathbf{u}^n \, d\mathbf{x} - \int_{\partial \Omega} \mathbf{v} \cdot (\hat{\mathbf{n}} \cdot (\nu \nabla \mathbf{u}^n)) \, d\mathbf{x} \quad (10)$$

$$= \int_{\Omega} \nu \nabla \mathbf{v} : \nabla \mathbf{u}^n \, d\mathbf{x} - \int_{\Gamma_N} \mathbf{v} \cdot (\hat{\mathbf{n}} \cdot (\nu \nabla \mathbf{u}^n)) \, d\mathbf{x} \quad (11)$$

since  $\mathbf{v} = 0$  on  $\Gamma_{D_1} \cup \Gamma_{D_2}$ . Furthermore, we have

$$\int_{\Omega} \mathbf{v} \cdot \nabla p^n \, d\mathbf{x} = - \int_{\Omega} (\nabla \cdot \mathbf{v}) p^n \, d\mathbf{x} + \int_{\partial \Omega} \mathbf{v} \cdot (\hat{\mathbf{n}} \cdot (p^n \mathbf{I})) \, d\mathbf{x} \quad (12)$$

$$= - \int_{\Omega} (\nabla \cdot \mathbf{v}) p^n \, d\mathbf{x} + \int_{\Gamma_N} \mathbf{v} \cdot (\hat{\mathbf{n}} \cdot (p^n \mathbf{I})) \, d\mathbf{x} \quad (13)$$

where once again, we have used  $\mathbf{v} = 0$  on  $\Gamma_{D_1} \cup \Gamma_{D_2}$ . Combining both the terms, we have

$$\int_{\Omega} \mathbf{v} \cdot [-\nu \Delta \mathbf{u}^n + \nabla p^n] \, d\mathbf{x} = \int_{\Omega} \nu \nabla \mathbf{v} : \nabla \mathbf{u}^n \, d\mathbf{x} - \int_{\Omega} (\nabla \cdot \mathbf{v}) p^n \, d\mathbf{x} - \int_{\Gamma_N} \mathbf{v} \cdot (\hat{\mathbf{n}} \cdot [-p^n \mathbf{I} + \nu \nabla \mathbf{u}^n]) \, d\mathbf{x} \quad (14)$$

$$= \int_{\Omega} \nu \nabla \mathbf{v} : \nabla \mathbf{u}^n \, d\mathbf{x} - \int_{\Omega} (\nabla \cdot \mathbf{v}) p^n \, d\mathbf{x} - \int_{\Gamma_N} \mathbf{v} \cdot \mathbf{h}^n \quad (15)$$

$$dxv. \quad (16)$$

Collating all terms, and using the inner product notation described in [Section 2.1](#), the Galerkin formulation of [\(6\)](#) is given by

$$(\mathbf{v}, \sigma \mathbf{u}^n) + (\mathbf{v}, \mathbf{u}^n \cdot \nabla \mathbf{u}^n) + s(\mathbf{v}, (\nabla \cdot \mathbf{u}^n) \mathbf{u}^n) + \nu (\nabla \mathbf{v}, \nabla \mathbf{u}^n) - (\nabla \cdot \mathbf{v}, p^n) + (q, \nabla \cdot \mathbf{u}^n) - (\mathbf{v}, \mathbf{g}^n) - (\mathbf{v}, \mathbf{h}^n)_{\Gamma_N} = 0 \quad (17)$$

for any  $\mathbf{v} \in \mathbf{V}$  and  $q \in Q$ .

### Lack of stability of the continuous Galerkin method

The continuous Galerkin formulation [\(17\)](#) of the NSE suffers from two major issues. The first issue relates to the saddle-point nature of the NSE, i.e., the absence of the pressure variable in the continuity equation. Because of this, only some special pairs of velocity and pressure functions are allowed. These pairs are called *inf-sup stable* pairs. However, a standard implementation of the Galerkin method using equal-order polynomials for both velocities and the pressure clearly violates this, and therefore, a stable numerical solution cannot be guaranteed [\[18, 4, 2\]](#).

The second issue relates to the presence of the advective term  $(\mathbf{u} \cdot \nabla) \mathbf{u}$ . The advection term has directional properties, and a continuous Galerkin formulation of this term is known to be unstable when advection dominates (compared to diffusion) [\[10, 19, 20\]](#).

There are multiple ways to resolve these two issues. The issue of instabilities due to non inf-sup conformity can be resolved by using methods such as PSPG [\[11, 12, 21\]](#) that remove the saddle point nature of the resulting FEM problem. The second issue can be resolved by using some kind of “upwinding”-type modification to the test function  $\mathbf{v}$  (e.g., SUPG [\[10\]](#)) or by using a least squares modifications to the FEM problem (e.g., GLS [\[19\]](#)) etc. In this work, we apply the variational multiscale method (VMS [\[14\]](#)) which provides both kinds of stability.

### 2.3 Stabilized formulation

The variational multiscale (VMS) method naturally addresses both instabilities discussed above in a consistent manner [\[17\]](#). Following [\[14, 17\]](#), we decompose the velocity and pressure at time step  $n$  as

$$\mathbf{u}^n(\mathbf{x}) = \mathbf{u}_h^n(\mathbf{x}) + \mathbf{u}_f^n(\mathbf{x}), \quad (18a)$$

$$p^n(\mathbf{x}) = p_h^n(\mathbf{x}) + p_f^n(\mathbf{x}). \quad (18b)$$

Here,  $(\mathbf{u}_h^n, p_h^n)$  denote the *coarse scales* represented by the finite element spaces, while  $(\mathbf{u}_f^n, p_f^n)$  denote the *fine scales* unresolved by the mesh. In residual-based VMS, the fine scales are modeled *element-wise* (and are generally discontinuous across element interfaces) in terms of the coarse-scale residuals.

**Note 1.** To streamline notation, we will drop the superscript  $n$  on  $(\mathbf{u}_h^n, \mathbf{u}_f^n, p_h^n, p_f^n)$  when no ambiguity arises, and write  $(\mathbf{u}_h, \mathbf{u}_f, p_h, p_f)$ .

Substituting [\(18\)](#) in [\(17\)](#), we obtain

$$(\mathbf{v}, \sigma(\mathbf{u}_h + \mathbf{u}_f)) + (\mathbf{v}, (\mathbf{u}_h + \mathbf{u}_f) \cdot \nabla(\mathbf{u}_h + \mathbf{u}_f)) + s(\mathbf{v}, (\nabla \cdot (\mathbf{u}_h + \mathbf{u}_f))(\mathbf{u}_h + \mathbf{u}_f)) + (\nabla \mathbf{v}, \nabla(\mathbf{u}_h + \mathbf{u}_f)) - (\nabla \cdot \mathbf{v}, p_h + p_f) + (q, \nabla \cdot (\mathbf{u}_h + \mathbf{u}_f)) - (\mathbf{v}, \mathbf{g}^n) - (\mathbf{v}, \mathbf{h}^n)_{\Gamma_N} = 0. \quad (19)$$

In this equation, both the coarse-scale variables  $(\mathbf{u}_h, p_h)$  and the fine-scale variables  $(\mathbf{u}_f, p_f)$  are unknown. In the residual-based VMS approach, the fine scales are modeled by

$$\mathbf{u}_f \approx \mathbf{u}' := -\tau_m \mathbf{R}_m, \quad (20a)$$

$$p_f \approx p' := -\tau_c \mathbf{R}_c, \quad (20b)$$

where the elementwise strong-form residuals are

$$\mathbf{R}_m := \sigma \mathbf{u}_h + \mathbf{u}_h \cdot \nabla \mathbf{u}_h + s(\nabla \cdot \mathbf{u}_h) \mathbf{u}_h - \nu \Delta \mathbf{u}_h + \nabla p_h - \mathbf{g}^n, \quad (21a)$$

$$\mathbf{R}_c := \nabla \cdot \mathbf{u}_h. \quad (21b)$$

The stabilization parameters  $\tau_m$  and  $\tau_c$  are also defined element-wise. For an element of characteristic size  $h$  they are computed as [22, 17]

$$\tau_m = \left[ \sigma^2 + \frac{c_1 |\mathbf{u}_h|^2}{h^2} + \frac{c_2 C_I \nu^2}{h^4} \right]^{-1/2}, \quad (22a)$$

$$\tau_c = \frac{c_3}{\tau_m} h^2, \quad (22b)$$

with constants  $c_1, c_2, c_3$  and inverse-estimate constant  $C_I$ . In this work, we assume  $\tau_m$  and  $\tau_c$  are constant within each element.

Substituting (20) into (19) yields

$$\begin{aligned} & (\mathbf{v}, \sigma(\mathbf{u}_h + \mathbf{u}')) + (\mathbf{v}, (\mathbf{u}_h + \mathbf{u}') \cdot \nabla(\mathbf{u}_h + \mathbf{u}')) + s(\mathbf{v}, (\nabla \cdot (\mathbf{u}_h + \mathbf{u}'))(\mathbf{u}_h + \mathbf{u}')) \\ & + (\nabla \mathbf{v}, \nabla(\mathbf{u}_h + \mathbf{u}')) - (\nabla \cdot \mathbf{v}, p_h + p') + (q, \nabla \cdot (\mathbf{u}_h + \mathbf{u}')) - (\mathbf{v}, \mathbf{g}^n) - (\mathbf{v}, \mathbf{h}^n)_{\Gamma_N} = 0. \end{aligned} \quad (23)$$

Because  $(\mathbf{u}', p')$  are defined element-wise, all terms involving  $\mathbf{u}'$  and  $p'$  in (23) are to be interpreted as elementwise integrals assembled over the mesh. Since  $(\mathbf{u}', p')$  are expressed in terms of  $(\mathbf{u}_h, p_h)$ , the only global unknowns are the coarse scales. Accordingly, we now restrict testing to the coarse-scale test spaces, giving the residual-based VMS formulation:

$$\begin{aligned} & (\mathbf{v}_h, \sigma(\mathbf{u}_h + \mathbf{u}')) + (\mathbf{v}_h, (\mathbf{u}_h + \mathbf{u}') \cdot \nabla(\mathbf{u}_h + \mathbf{u}')) + s(\mathbf{v}_h, (\nabla \cdot (\mathbf{u}_h + \mathbf{u}'))(\mathbf{u}_h + \mathbf{u}')) \\ & + (\nabla \mathbf{v}_h, \nabla(\mathbf{u}_h + \mathbf{u}')) - (\nabla \cdot \mathbf{v}_h, p_h + p') + (q_h, \nabla \cdot (\mathbf{u}_h + \mathbf{u}')) - (\mathbf{v}_h, \mathbf{g}^n) - (\mathbf{v}_h, \mathbf{h}^n)_{\Gamma_N} = 0. \end{aligned} \quad (24)$$

### 2.3.1 Derivatives of the fine scale velocities

Equation (24) involves spatial derivatives of the modeled fine-scale velocity  $\mathbf{u}'$ . This is problematic because differentiating  $\mathbf{u}' = -\tau_m \mathbf{R}_m$  introduces derivatives of both the residual and the stabilization parameter. For example,

$$\frac{\partial \mathbf{u}'}{\partial x_i} = \frac{\partial}{\partial x_i} (-\tau_m \mathbf{R}_m) = - \left[ \mathbf{R}_m \frac{\partial \tau_m}{\partial x_i} + \tau_m \frac{\partial \mathbf{R}_m}{\partial x_i} \right]. \quad (25)$$

The first term contains

$$\frac{\partial \tau_m}{\partial x_i} = -\frac{1}{2} \left[ \sigma^2 + \frac{c_1 |\mathbf{u}_h|^2}{h^2} + \frac{c_2 C_I \nu^2}{h^4} \right]^{-3/2} \times \left[ \frac{2c_1}{h^2} \mathbf{u}_h \cdot \frac{\partial \mathbf{u}_h}{\partial x_i} \right], \quad (26)$$

which is already nonlinear in  $\mathbf{u}_h$ . The second term contains

$$\frac{\partial \mathbf{R}_m}{\partial x_i} = \frac{\partial}{\partial x_i} [\sigma \mathbf{u}_h + \mathbf{u}_h \cdot \nabla \mathbf{u}_h + s(\nabla \cdot \mathbf{u}_h) \mathbf{u}_h - \nu \Delta \mathbf{u}_h + \nabla p_h - \mathbf{g}^n], \quad (27)$$

which involves third derivatives of  $\mathbf{u}_h$ , second derivatives of  $p_h$ , and derivatives of  $\mathbf{g}^n$ . These differentiability requirements exceed those of the original weak form and are generally incompatible with low-order continuous finite element spaces. For this reason, practical residual-based VMS implementations typically avoid explicit differentiation of  $\mathbf{R}_m$  and  $\tau_m$  (and often assume  $\tau_m$  and  $\tau_c$  are constant within each element, as we do here). The remaining difficulty is then how to rewrite the weak form so that  $\mathbf{u}'$  appears without derivatives.

In (24), derivatives act on  $\mathbf{u}'$  through three terms: the continuity term, the diffusion term, and the convection term. We next consider each.

- **Continuity term:** The term  $(q_h, \nabla \cdot (\mathbf{u}_h + \mathbf{u}'))$  can be treated by integration by parts, which transfers derivatives onto the test function:

$$(q_h, \nabla \cdot (\mathbf{u}_h + \mathbf{u}')) = (q_h, \nabla \cdot \mathbf{u}_h) + (q_h, \nabla \cdot \mathbf{u}') = (q_h, \nabla \cdot \mathbf{u}_h) - (\nabla q_h, \mathbf{u}') + (q_h, \hat{\mathbf{n}} \cdot \mathbf{u}')_{\partial\Omega}.$$

- **Diffusion term:** The diffusion contribution produces  $(\nabla \mathbf{v}_h, \nabla \mathbf{u}')$ , for which transferring derivatives off  $\mathbf{u}'$  is not straightforward in low-order settings. In much of the VMS literature this term is therefore dropped, i.e.,

$$(\nabla \mathbf{v}_h, \nabla (\mathbf{u}_h + \mathbf{u}')) \approx (\nabla \mathbf{v}_h, \nabla \mathbf{u}_h).$$

Since the Laplacian with Dirichlet conditions is coercive, this modification is commonly justified by viewing  $\mathbf{u}_h$  as a Riesz projection of  $\mathbf{u}$ , so that omitting  $(\nabla \mathbf{v}_h, \nabla \mathbf{u}')$  does not compromise diffusion stability.

- **Convection term:** The convection contribution is more delicate: it cannot be discarded without affecting stability, and it is the primary source of formulation-dependent manipulations in nonlinear residual-based VMS. Moreover, the specific weakening steps depend on whether convection is written in convective form ( $s = 0$ ) or divergence form ( $s = 1$ ), and they introduce different boundary flux terms.

1. *Case  $s = 1$  (divergence form):* Using integration by parts,

$$(\mathbf{v}_h, \nabla \cdot ((\mathbf{u}_h + \mathbf{u}')( \mathbf{u}_h + \mathbf{u}')^T)) = -(\nabla \mathbf{v}_h, (\mathbf{u}_h + \mathbf{u}')( \mathbf{u}_h + \mathbf{u}')^T) + \\ (\mathbf{v}_h, \hat{\mathbf{n}} \cdot [(\mathbf{u}_h + \mathbf{u}')( \mathbf{u}_h + \mathbf{u}')^T])_{\partial\Omega}.$$

2. *Case  $s = 0$  (convective form):* A common manipulation is to add and subtract a term based on the modeling interpretation that  $(\mathbf{u}_h + \mathbf{u}')$  represents the full velocity and should therefore be (approximately) solenoidal. Specifically, one introduces  $\nabla \cdot (\mathbf{u}_h + \mathbf{u}') \mathbf{u}'$  under the integral to rewrite

$$(\mathbf{v}_h, (\mathbf{u}_h + \mathbf{u}') \cdot \nabla (\mathbf{u}_h + \mathbf{u}')) = (\mathbf{v}_h, (\mathbf{u}_h + \mathbf{u}') \cdot \nabla (\mathbf{u}_h + \mathbf{u}')) + (\mathbf{v}_h, \nabla \cdot (\mathbf{u}_h + \mathbf{u}') \mathbf{u}') \\ = (\mathbf{v}_h, (\mathbf{u}_h + \mathbf{u}') \cdot \nabla \mathbf{u}_h) + (\mathbf{v}_h, \nabla \cdot [\mathbf{u}' (\mathbf{u}_h + \mathbf{u}')^T]) \\ = (\mathbf{v}_h, (\mathbf{u}_h + \mathbf{u}') \cdot \nabla \mathbf{u}_h) - (\nabla \mathbf{v}_h, \mathbf{u}' (\mathbf{u}_h + \mathbf{u}')^T) \\ + (\mathbf{v}_h, \hat{\mathbf{n}} \cdot [\mathbf{u}' (\mathbf{u}_h + \mathbf{u}')^T])_{\partial\Omega}.$$

**Remark 2.1.** The two convection treatments differ by the volume term  $(\mathbf{v}_h, (\nabla \cdot (\mathbf{u}_h + \mathbf{u}')) \mathbf{u}_h)$  and by the form of the resulting boundary flux contributions. While these boundary terms vanish under full Dirichlet conditions on  $\partial\Omega$ , they do not generally vanish when mixed boundary conditions are present. Consequently, the weakening steps used to avoid derivatives of  $\mathbf{u}'$  can be sensitive to the boundary partition and to how boundary integrals are treated numerically.

**Remark 2.2.** The preceding discussion motivates the central question addressed in the next section: can one obtain a residual-based VMS formulation in which the unresolved-scale velocity enters the weak form without derivatives, *without* relying on case-dependent manipulations of the nonlinear convection term? As we will show, linearizing convection (so the convecting velocity is known) enables an exact adjoint operator, which provides a systematic way to transfer derivatives from unresolved-scale terms onto test functions.

### 3 Linear semi-implicit variational formulation

The discussion in [Section 2](#) shows that, in nonlinear residual-based VMS for the incompressible NSE, avoiding spatial derivatives of the modeled fine scales typically requires additional manipulations that depend on the chosen convection form and may introduce boundary-condition-sensitive flux terms. In this section, we present a semi-implicit formulation that avoids such case-dependent steps for the convection contribution. The key device is to replace the nonlinear convection velocity by a known convecting field, leading to an Oseen-type problem. For this linear convection operator, an exact adjoint can be written, enabling a systematic transfer of derivatives onto test functions.

### 3.1 Oseen equations with generalized convection

The Oseen equations are a linear approximation of the Navier–Stokes equations in which the convecting velocity is prescribed. In (6), the unknown velocity  $\mathbf{u}^n$  is transported by itself. The Oseen approximation replaces this convecting velocity by a known field  $\mathbf{a}$ , yielding a linear problem for  $(\mathbf{u}^n, p^n)$ :

$$\sigma \mathbf{u}^n + \mathcal{M}_{\mathbf{a},s} \mathbf{u}^n - \nu \Delta \mathbf{u}^n + \nabla p^n - \mathbf{g}^n = \mathbf{0}, \quad (28a)$$

$$\nabla \cdot \mathbf{u}^n = 0, \quad (28b)$$

with the same boundary conditions as in (2). Here  $s \in \{0, \frac{1}{2}, 1\}$  parameterizes three common linear advection forms. We define the generalized linear advection operator

$$\mathcal{M}_{\mathbf{a},s} \mathbf{u} := (\mathbf{a} \cdot \nabla) \mathbf{u} + s(\nabla \cdot \mathbf{a}) \mathbf{u}. \quad (29)$$

For  $s = 0, \frac{1}{2}, 1$  this recovers the convective, skew-symmetric, and divergence linear forms, summarized in Table 1. Unlike the nonlinear operator  $\mathcal{M}_{\mathbf{u},s} \mathbf{u}$ , the operator (29) is linear in  $\mathbf{u}$  and admits an exact adjoint in the weak form, which is central to what follows.

In a time-marching context,  $\mathbf{a}$  is obtained by backward extrapolation from previously computed coarse-scale velocities:

$$\mathbf{a} = \begin{cases} \mathbf{u}_h^{n-1}, & \text{(first-order extrapolation),} \\ 2\mathbf{u}_h^{n-1} - \mathbf{u}_h^{n-2}, & \text{(second-order extrapolation).} \end{cases} \quad (30)$$

The resulting method is *semi-implicit*: convection is treated explicitly through  $\mathbf{a}$ , while diffusion and pressure remain implicit.

Table 1:  $\mathcal{M}_{\mathbf{a},s} \mathbf{u} = (\mathbf{a} \cdot \nabla) \mathbf{u} + s(\nabla \cdot \mathbf{a}) \mathbf{u}$ , for three chosen values of  $s$ .

$s$	Operator symbol	Descriptive name	Expression	
			Vector notation	Index notation
0	$C_{\mathbf{a}} := \mathcal{M}_{\mathbf{a},0}$	Convective form	$(\mathbf{a} \cdot \nabla) \mathbf{u}$	$(a_j \partial_j) u_i$
$\frac{1}{2}$	$S_{\mathbf{a}} := \mathcal{M}_{\mathbf{a},\frac{1}{2}}$	Skew-symmetric form	$(\mathbf{a} \cdot \nabla) \mathbf{u} + \frac{1}{2}(\nabla \cdot \mathbf{a}) \mathbf{u}$	$(a_j \partial_j) u_i + \frac{1}{2}(\partial_j a_j) u_i$
1	$D_{\mathbf{a}} := \mathcal{M}_{\mathbf{a},1}$	Divergence form	$\nabla \cdot (\mathbf{u} \mathbf{a}^T)$	$\partial_j (u_i a_j)$

#### 3.1.1 Variational identity and exact adjoint

The operator  $\mathcal{M}_{\mathbf{a},s}$  has the property that, when tested against a sufficiently smooth  $\mathbf{v}$ , all derivatives acting on  $\mathbf{u}$  can be transferred to  $\mathbf{v}$  exactly.

**Proposition 1.** (Exact adjoint relation for  $\mathcal{M}_{\mathbf{a},s}$ ) Let  $\mathbf{a}$  be sufficiently smooth and let  $\mathbf{u}, \mathbf{v}$  be sufficiently smooth vector fields with well-defined traces on  $\partial\Omega$ . Then

$$(\mathbf{v}, \mathcal{M}_{\mathbf{a},s} \mathbf{u}) = (-\mathcal{M}_{\mathbf{a},1-s} \mathbf{v}, \mathbf{u}) + (\mathbf{v}, \hat{\mathbf{n}} \cdot (\mathbf{u} \mathbf{a}^T))_{\partial\Omega}. \quad (31)$$

*Proof.* Using  $\nabla \cdot (\mathbf{u} \mathbf{a}^T) = (\mathbf{a} \cdot \nabla) \mathbf{u} + (\nabla \cdot \mathbf{a}) \mathbf{u}$ , we write

$$\begin{aligned} (\mathbf{v}, \mathcal{M}_{\mathbf{a},s} \mathbf{u}) &= (\mathbf{v}, (\mathbf{a} \cdot \nabla) \mathbf{u} + s(\nabla \cdot \mathbf{a}) \mathbf{u}) \\ &= (\mathbf{v}, \nabla \cdot (\mathbf{u} \mathbf{a}^T)) + (s-1)(\mathbf{v}, (\nabla \cdot \mathbf{a}) \mathbf{u}) \\ &= -(\nabla \mathbf{v}, \mathbf{u} \mathbf{a}^T) + (\mathbf{v}, \hat{\mathbf{n}} \cdot (\mathbf{u} \mathbf{a}^T))_{\partial\Omega} + (s-1)((\nabla \cdot \mathbf{a}) \mathbf{v}, \mathbf{u}) \\ &= -((\mathbf{a} \cdot \nabla) \mathbf{v}, \mathbf{u}) - (1-s)((\nabla \cdot \mathbf{a}) \mathbf{v}, \mathbf{u}) + (\mathbf{v}, \hat{\mathbf{n}} \cdot (\mathbf{u} \mathbf{a}^T))_{\partial\Omega} \\ &= (-\mathcal{M}_{\mathbf{a},1-s} \mathbf{v}, \mathbf{u}) + (\mathbf{v}, \hat{\mathbf{n}} \cdot (\mathbf{u} \mathbf{a}^T))_{\partial\Omega}. \end{aligned}$$

■

**Remark 3.1.** Proposition 1 is the key mechanism that removes case-by-case weakening for the *convection* contribution in residual-based VMS: once convection is linearized, the exact adjoint transfers derivatives onto the test functions in a uniform way for all  $s \in \{0, \frac{1}{2}, 1\}$ . In particular, convection-related terms can be written without requiring spatial derivatives of the modeled fine-scale velocity  $u'$ .

**Remark 3.2.** If we take  $\mathbf{v}$  to be an infinitely smooth function with compact support in  $\Omega$  (i.e.,  $\mathbf{v}$  and its derivatives vanish near  $\partial\Omega$ ), then the boundary term in (31) vanishes, and we have

$$(\mathbf{v}, \mathcal{M}_{\mathbf{a},s} \mathbf{u}) = -(\mathcal{M}_{\mathbf{a},1-s} \mathbf{v}, \mathbf{u}). \quad (32)$$

The operator acting on  $\mathbf{v}$  is the adjoint operator of  $\mathcal{M}_{\mathbf{a},s}$ , and is denoted by  $\mathcal{M}_{\mathbf{a},s}^*$ . So, we have

$$\mathcal{M}_{\mathbf{a},s}^* = -\mathcal{M}_{\mathbf{a},1-s}.$$

Table 2 summarizes the adjoint expressions for each value of  $s \in \{0, \frac{1}{2}, 1\}$ .

Table 2: Summary of  $\mathcal{M}_{\mathbf{a},s}$  and  $\mathcal{M}_{\mathbf{a},s}^*$

$s$	Descriptive name	Operator expression $\mathcal{M}_{\mathbf{a},s} \mathbf{u}$	Adjoint expression $\mathcal{M}_{\mathbf{a},s}^* \mathbf{v}$
0	Convective form	$(\mathbf{a} \cdot \nabla) \mathbf{u}$	$-\nabla \cdot (\mathbf{v} \mathbf{a}^T)$
$\frac{1}{2}$	Skew-symmetric form	$(\mathbf{a} \cdot \nabla) \mathbf{u} + \frac{1}{2}(\nabla \cdot \mathbf{a}) \mathbf{u}$	$-[(\mathbf{a} \cdot \nabla) \mathbf{v} + \frac{1}{2}(\nabla \cdot \mathbf{a}) \mathbf{v}]$
1	Divergence form	$\nabla \cdot (\mathbf{u} \mathbf{a}^T)$	$-(\mathbf{a} \cdot \nabla) \mathbf{v}$

### 3.2 Stabilized formulation of the Oseen equations

The Oseen system (28) exhibits the same saddle-point and convection-driven instabilities as the nonlinear NSE, so we again apply residual-based VMS. The Galerkin weak form of (28) reads: find  $(\mathbf{u}^n, p^n) \in \mathbf{V}^D \times Q$  such that for all  $(\mathbf{v}, q) \in \mathbf{V} \times Q$ ,

$$(\mathbf{v}, \sigma \mathbf{u}^n) + (\mathbf{v}, \mathcal{M}_{\mathbf{a},s} \mathbf{u}^n) + \nu (\nabla \mathbf{v}, \nabla \mathbf{u}^n) - (\nabla \cdot \mathbf{v}, p^n) + (q, \nabla \cdot \mathbf{u}^n) - (\mathbf{v}, \mathbf{g}^n) - (\mathbf{v}, \mathbf{h}^n)_{\Gamma_N} = 0. \quad (33)$$

Using Proposition 1 and  $\mathbf{v} = \mathbf{0}$  on  $\Gamma_{D_1} \cup \Gamma_{D_2}$ , we obtain

$$(\mathbf{v}, \sigma \mathbf{u}^n) - (\mathcal{M}_{\mathbf{a},1-s} \mathbf{v}, \mathbf{u}^n) + \nu (\nabla \mathbf{v}, \nabla \mathbf{u}^n) - (\nabla \cdot \mathbf{v}, p^n) + (q, \nabla \cdot \mathbf{u}^n) + (\mathbf{v}, \hat{\mathbf{n}} \cdot (\mathbf{u}^n \mathbf{a}^T))_{\Gamma_N} - (\mathbf{v}, \mathbf{g}^n) - (\mathbf{v}, \mathbf{h}^n)_{\Gamma_N} = 0. \quad (34)$$

We now apply the VMS decomposition

$$\mathbf{u}^n = \mathbf{u}_h + \mathbf{u}_f, \quad (35a)$$

$$p^n = p_h + p_f, \quad (35b)$$

and model the fine scales element-wise as

$$\mathbf{u}_f \approx \mathbf{u}' := -\tau_m \mathbf{R}_m, \quad (36a)$$

$$p_f \approx p' := -\tau_c \mathbf{R}_c, \quad (36b)$$

with elementwise residuals of the Oseen strong form

$$\mathbf{R}_m := \sigma \mathbf{u}_h + \mathcal{M}_{\mathbf{a},s} \mathbf{u}_h - \nu \Delta \mathbf{u}_h + \nabla p_h - \mathbf{g}^n, \quad (37a)$$

$$\mathbf{R}_c := \nabla \cdot \mathbf{u}_h. \quad (37b)$$

Substituting into (34) gives

$$\begin{aligned} (\mathbf{v}, \sigma(\mathbf{u}_h + \mathbf{u}')) - (\mathcal{M}_{\mathbf{a},1-s}\mathbf{v}, (\mathbf{u}_h + \mathbf{u}')) + \nu (\nabla \mathbf{v}, \nabla(\mathbf{u}_h + \mathbf{u}')) - (\nabla \cdot \mathbf{v}, p_h + p') \\ + (q, \nabla \cdot (\mathbf{u}_h + \mathbf{u}')) + (\mathbf{v}, \hat{\mathbf{n}} \cdot ((\mathbf{u}_h + \mathbf{u}') \mathbf{a}^T))_{\Gamma_N} - (\mathbf{v}, \mathbf{g}^n) - (\mathbf{v}, \mathbf{h}^n)_{\Gamma_N} = 0. \end{aligned} \quad (38)$$

As in [Section 2.3.1](#), we avoid derivatives of the modeled fine scales in the diffusion and continuity contributions by (i) dropping  $(\nabla \mathbf{v}, \nabla \mathbf{u}')$  and (ii) integrating  $(q, \nabla \cdot \mathbf{u}')$  by parts. Restricting test functions to the coarse-scale test spaces  $(\mathbf{v}_h, q_h)$  yields the stabilized semi-implicit Oseen–VMS formulation:

$$\begin{aligned} (\mathbf{v}_h, \sigma(\mathbf{u}_h + \mathbf{u}')) - (\mathcal{M}_{\mathbf{a},1-s}\mathbf{v}_h, (\mathbf{u}_h + \mathbf{u}')) + \nu (\nabla \mathbf{v}_h, \nabla \mathbf{u}_h) - (\nabla \cdot \mathbf{v}_h, p_h + p') \\ + (q_h, \nabla \cdot \mathbf{u}_h) - (\nabla q_h, \mathbf{u}') + (\mathbf{v}_h, \hat{\mathbf{n}} \cdot ((\mathbf{u}_h + \mathbf{u}') \mathbf{a}^T))_{\Gamma_N} - (\mathbf{v}_h, \mathbf{g}^n) - (\mathbf{v}_h, \mathbf{h}^n)_{\Gamma_N} = 0. \end{aligned} \quad (39)$$

Equation (39) is a semi-implicit stabilized formulation obtained from an Oseen approximation. It can be viewed as a linear counterpart of (24). Two features distinguish it from the fully implicit nonlinear VMS form. First, linearization of the convection operator makes its adjoint available in closed form, so the convection contribution can be written in a uniform weak form for all  $s \in \{0, \frac{1}{2}, 1\}$  without case-by-case weakening of fine-scale convection terms. Second, the resulting time-marching method is linear at each step and therefore requires only one linear solve per time step, which yields substantial savings relative to fully implicit nonlinear VMS formulations. In the next section we specify the algorithmic ingredients needed to realize Eqn (39).

## 4 Implementation details

The semi-implicit VMS formulation (39) requires only standard continuous Galerkin ingredients (Lagrange basis functions, elementwise residual evaluation, and elementwise stabilization parameters) and can be incorporated into existing FEM codebases. All numerical experiments in this paper are produced with an in-house MPI-based parallel finite element code written in C/C++. Mesh partitioning is performed with `PARMETIS` [23]. Parallel sparse linear algebra and solvers are provided by `PETSc` [24].

For the linear semi-implicit formulation, the algebraic system at each time step is solved with a Krylov method (KSP) using BCGS together with an additive Schwarz preconditioner (ASM). For the fully implicit nonlinear formulation, we use `PETSc` SNES; each Newton step is solved using the same Krylov and preconditioning options (BCGS+ASM). Additional details on the parallelization strategy and performance characteristics of the software can be found in [25, 26, 27]. Unless stated otherwise, identical solver tolerances are used when comparing linear and nonlinear variants, so that reported timing differences reflect the algorithmic cost rather than the stopping criteria.

## 5 Numerical results

This section evaluates the semi-implicit stabilized formulation introduced in [Section 3](#). A central practical question is how the choice of advection form affects robustness and accuracy. Accordingly, we compare three linear semi-implicit methods corresponding to  $s \in \{0, \frac{1}{2}, 1\}$  and two fully implicit nonlinear VMS methods corresponding to  $s \in \{0, 1\}$ . Across all methods we report (i) temporal accuracy on a manufactured solution, (ii) benchmark accuracy on canonical laminar flows, (iii) performance on representative three-dimensional turbulent flows, and (iv) computational cost relative to fully implicit nonlinear VMS.

### 5.1 Convergence study

We begin by testing the convergence of the method proposed in (39) by examining how the errors behave with respect to the time-step size  $\Delta t$ . We take the exact solution  $(\mathbf{u}, p)$  to be

$$\mathbf{u} = \begin{bmatrix} \sin(\pi x) \cos(\pi y) \sin(\pi t) \\ -\cos(\pi x) \sin(\pi y) \sin(\pi t) \end{bmatrix}, \quad (40a)$$

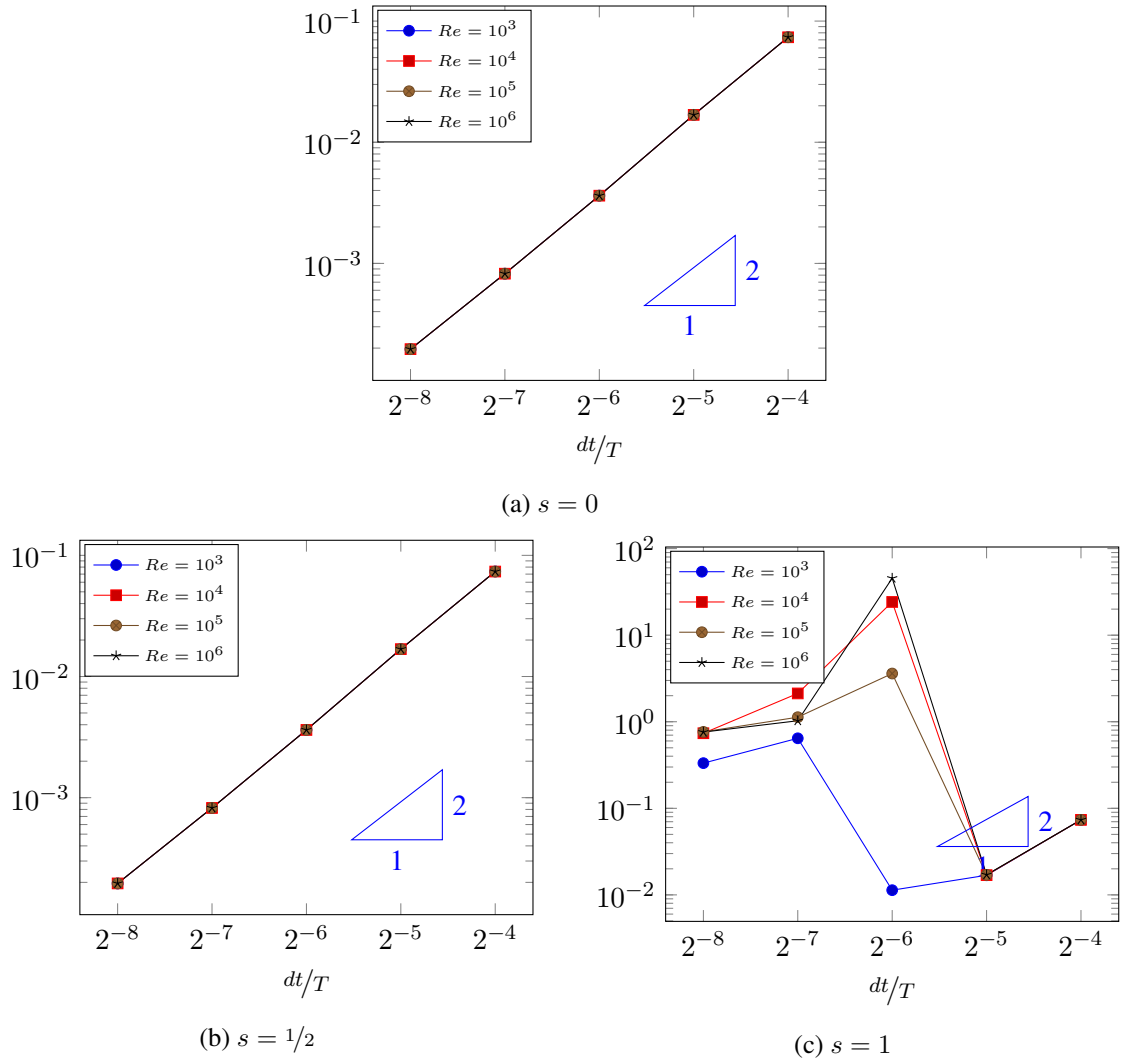


Figure 2: Convergence of  $\|u_x^h - u_x\|_{L^2(\Omega)}$  with the semi-implicit methods ( $T = 2.5$ ).

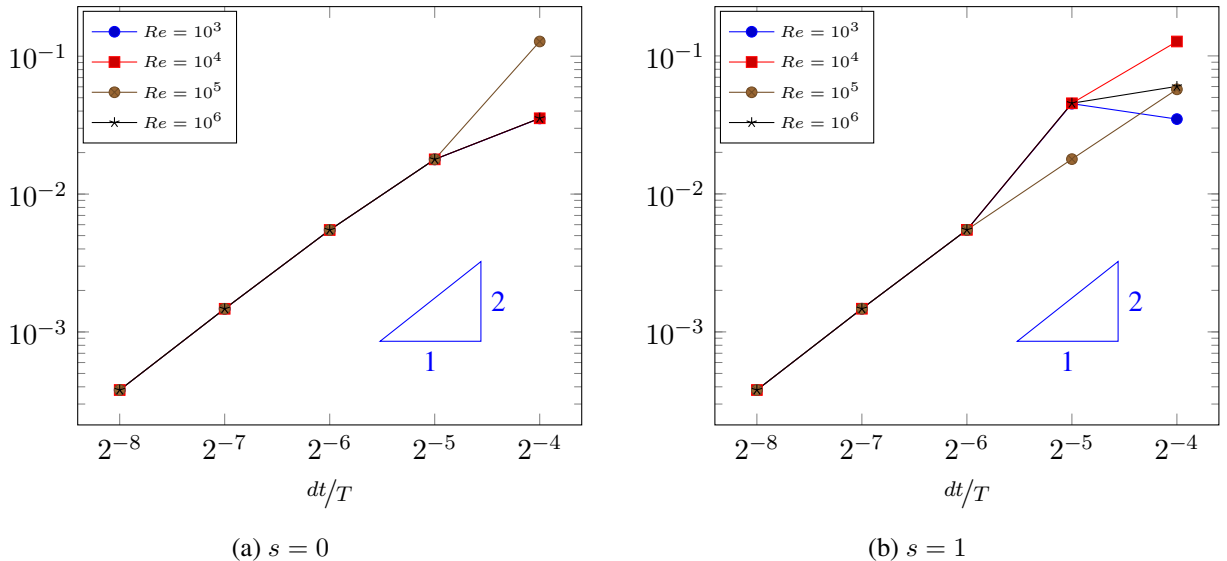


Figure 3: Convergence of  $\|u_x^h - u_x\|_{L^2(\Omega)}$  with the nonlinear methods  $T = 2.5$ .

$$p = \sin(\pi x) \sin(\pi y) \cos(\pi t) \quad (40b)$$

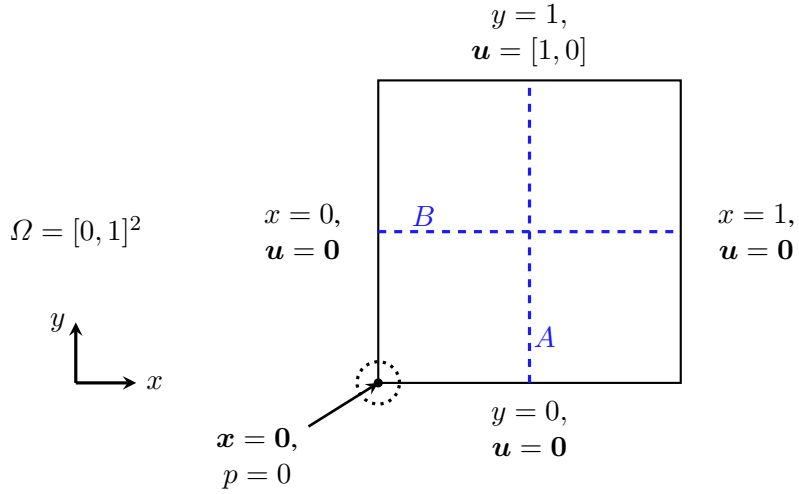


Figure 4: Boundary conditions for the lid-driven cavity problem. The blue dashed lines are the midlines where velocities will be evaluated and plotted (see [Figure 5](#))

in a unit square domain, i.e.,  $\Omega = [0, 1]^2$ . The velocity  $\mathbf{u}$  is chosen such that it satisfies  $\nabla \cdot \mathbf{u} = 0$  exactly pointwise. We obtain the symbolic / analytical expression for the forcing  $\mathbf{f}$  by substituting the exact solutions  $(\mathbf{u}, p)$  in [\(1\)](#). We also analytically obtain the initial condition  $\mathbf{u}_0$  by setting  $t = 0$  in [\(40\)](#), and the boundary condition  $\mathbf{u}_d$  on all sides by setting  $\mathbf{x} = (x, y)$  appropriately.

Once we have the expressions for  $\mathbf{f}$ ,  $\mathbf{u}_0$  and  $\mathbf{u}_d$ , we solve [\(1\)](#) using the proposed numerical method [\(39\)](#), and obtain the approximate solutions  $(\mathbf{u}_h, p_h)$ . Finally, we measure the error in  $(\mathbf{u}_h, p_h)$  with respect to the exact solution  $(\mathbf{u}, p)$  using

$$\|e\|(t) = \left[ \int_{\Omega} (\mathbf{u}_h(t) - \mathbf{u}(t))^2 \, d\mathbf{x} \right]^{1/2}. \quad (41)$$

[Figure 2](#) shows the convergence of  $u_x$  as the step size  $\Delta t$  is varied from  $\Delta t = T/8$  to  $\Delta t = T/256$ , for  $s = 0, 0.5, 1$ . The time discretization is BDF2, so we expect an order of convergence of 2. This order of convergence is achieved for  $s = 0$  and  $s = 0.5$ . However,  $s = 1$  exhibits an unstable behavior, and errors do not necessarily decrease when the time step is reduced. For reference, [Figure 3](#) presents the same convergence study for the nonlinear methods for both  $s = 0, 1$ . Both formulations show an order of convergence of 2 as  $\Delta t$  is reduced.

## 5.2 Lid driven cavity (2D)

[Figure 4](#) shows a schematic of the lid-driven cavity problem in 2D. The computational domain is  $\Omega = [0, 1]^2$ . The boundary conditions are static (do not change with time) and are given by

$$\mathbf{u} = \mathbf{0}, \quad y = 0, \quad (42a)$$

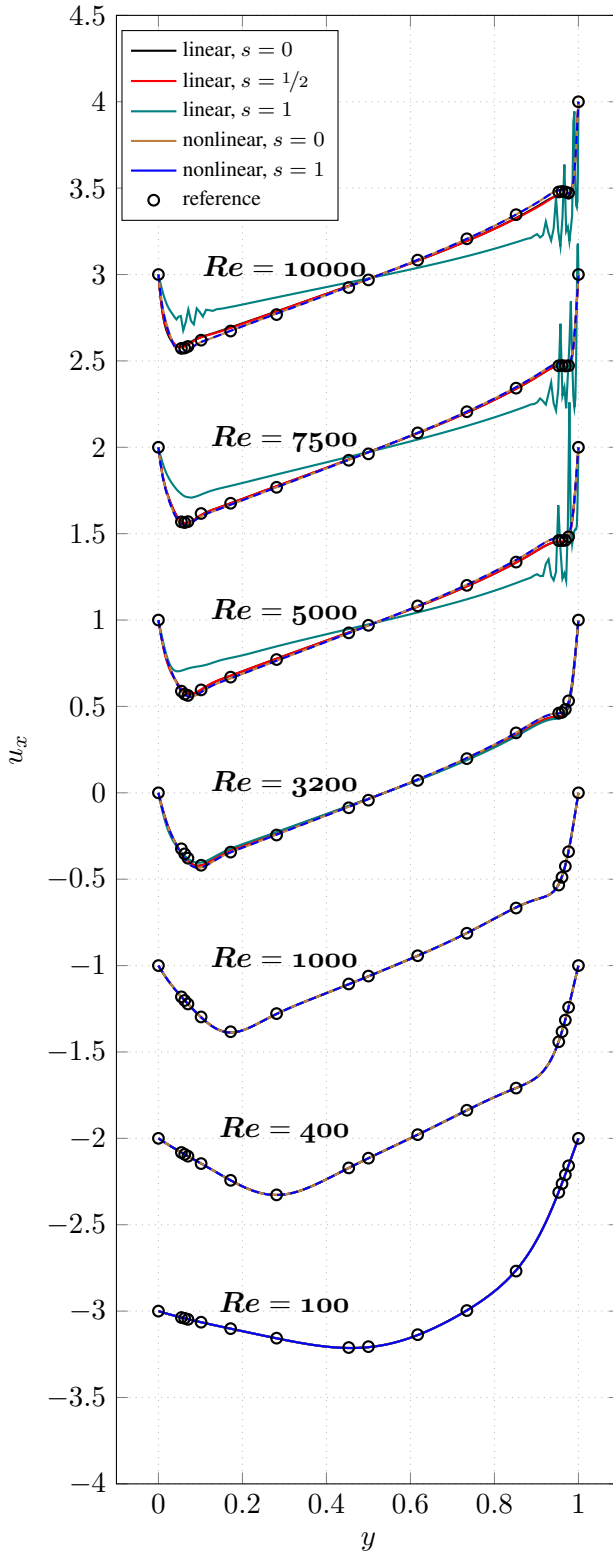
$$\mathbf{u} = [1, 0]^T, \quad y = 1, \quad (42b)$$

$$\mathbf{u} = \mathbf{0} \quad x \in \{0, 1\}. \quad (42c)$$

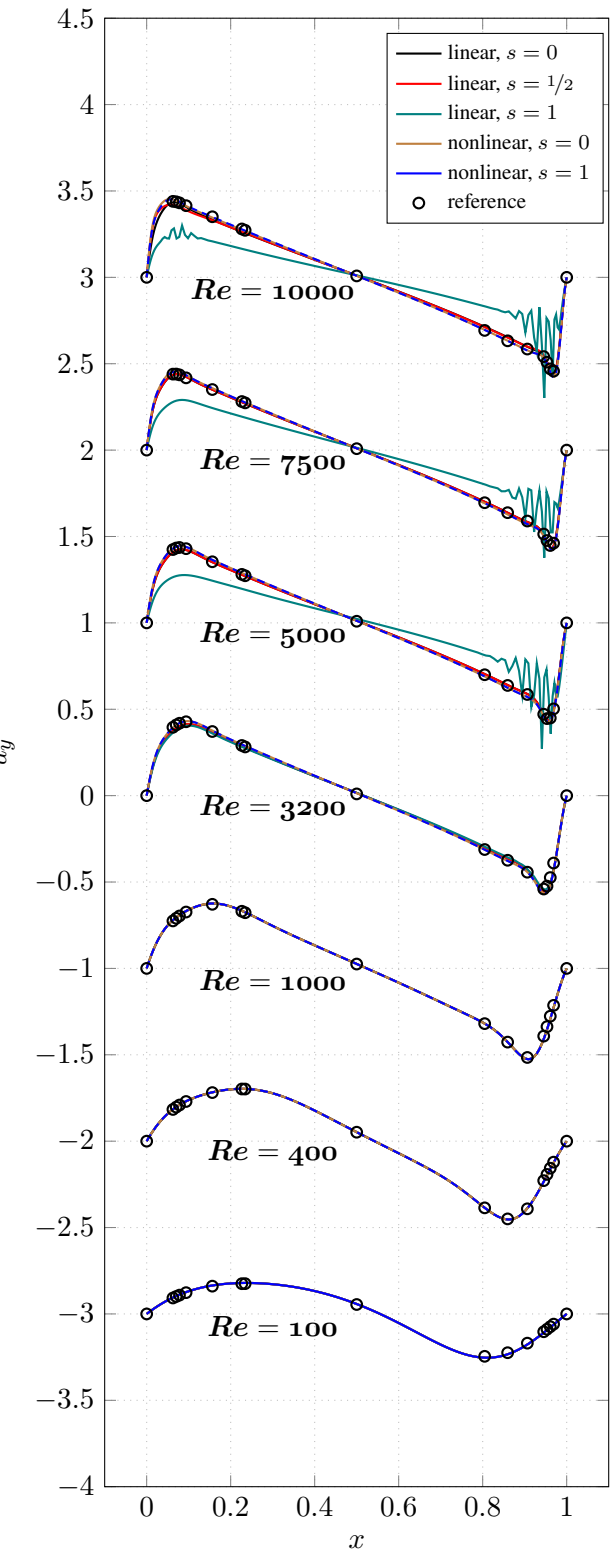
The boundary condition comprise a ‘‘lid’’ at the top moving with horizontal velocity = 1, and no-slip walls on the rest of the three sides. The forcing  $\mathbf{f} = \mathbf{0}$ , and the initial condition is given by a zero function

$$\mathbf{u}_0 = \mathbf{0}. \quad (43)$$

We solve this problem for a series of Reynolds numbers  $Re = 100, 400, 1000, 3200, 5000, 7500$  and  $10000$ . The benchmark results for this problem generally refer to the steady-state solution. Suppose  $\partial_t \mathbf{u} = \mathbf{0}$ ,  $\partial_t p = 0$  for some  $t \geq t_s$ . Then the final time horizon  $T$  is chosen such that  $T > t_s$ . Usually  $t_s$  increases with an increase in the Reynolds number. Here, we choose  $T = 5 \times 10^3$  for all cases.



(a)  $x$ -constant line



(b)  $y$ -constant line

Figure 5: Midline velocity profiles for the lid-driven cavity problem (see Section 5.2 and Figure 4) at  $t = T$  for different Reynolds numbers. Left column shows  $u_x(x = 0.5, y, t = T)$  against  $y$ , whereas right column shows  $u_y(x, y = 0.5, t = T)$  against  $x$ . Curves for different  $Re$  are shifted successively by one unit in the vertical direction for clarity. Results from Ghia et al. [28] included for comparison (shown in markers).

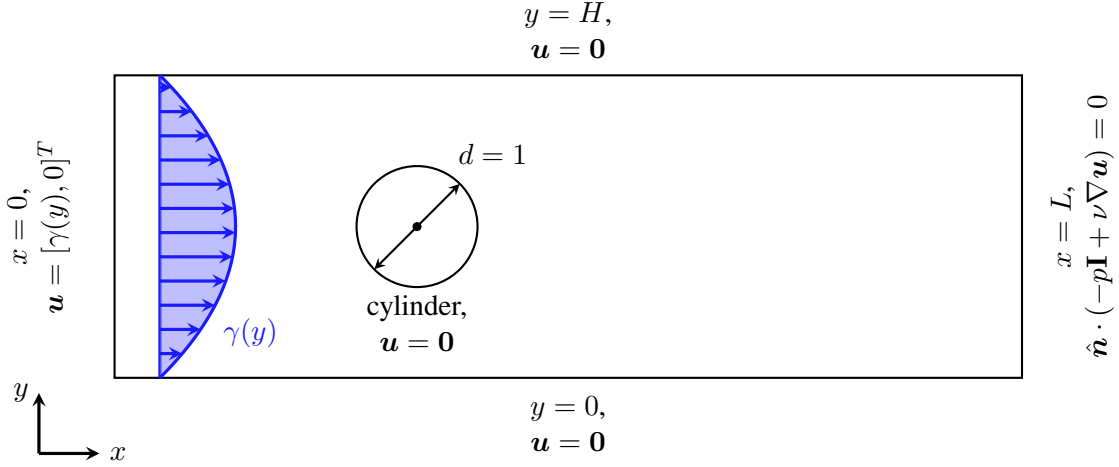


Figure 6: Schematic diagram of the flow past a circular cylinder in 2D. The inlet velocity profile  $\gamma(y)$  is shown in blue curves and text.

Figure 5 plots the standard midline velocity profiles for all the considered Reynolds numbers for nonlinear  $s = 0, 1$  and linear  $s = 0, 1/2, 1$ . Figure 5a shows the  $x$ -component of the velocity ( $u_x$ ) on the  $x = 0.5$  vertical line (line ‘A’ in Figure 4). And similarly, Figure 5b plots the  $y$ -component of the velocity ( $u_y$ ) on the  $y = 0.5$  horizontal line (line ‘B’ in Figure 4).

We see that the linear methods with  $s = 0, 1/2$ , and the nonlinear methods with  $s = 0, 1$  are all in good agreement with the reference values. The linear method with  $s = 1$  behaves well for low Reynolds numbers, but incurs spatial oscillations for the higher Reynolds number (above  $Re = 3200$ ), thereby losing accuracy.

### 5.3 Flow past a circular cylinder (2D)

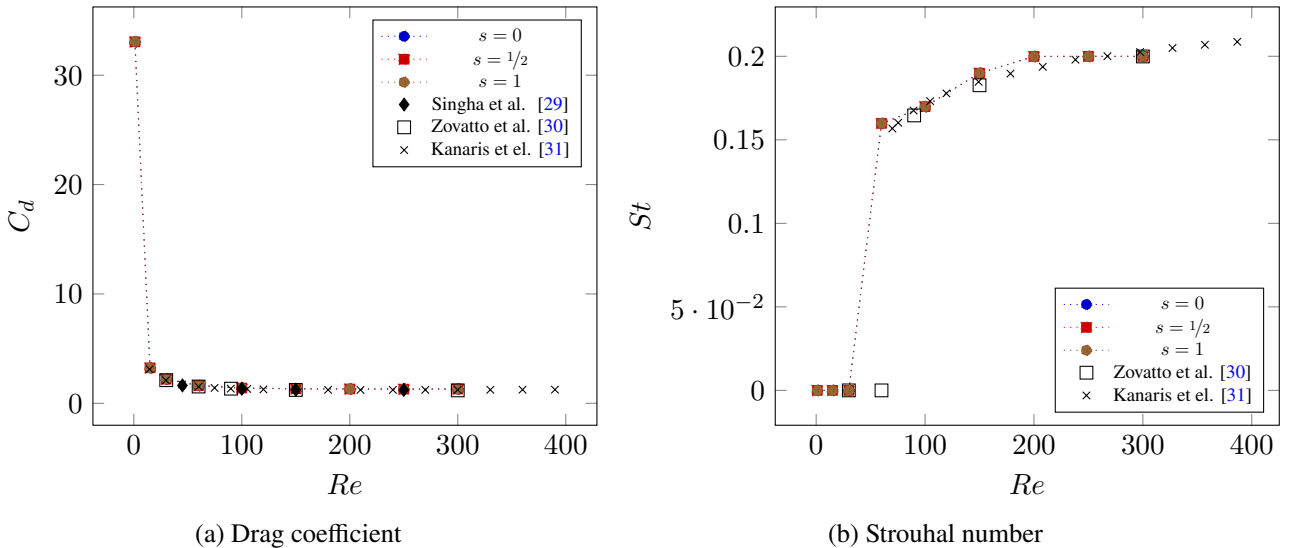


Figure 7: Results for flow past a circular cylinder in two spatial dimensions: (a) Drag coefficient  $C_d$ , (b) Strouhal number  $St$

Next, we test our method on the problem of two-dimensional flow past a circular cylinder. The setup is taken from [32, 31, 30]. The schematic of the problem is shown in Figure 6. The spatial domain is  $\Omega = ((I_x \times I_y) \setminus C)$ , where  $I_x = [0, L]$ ,  $I_y = [0, H]$  and  $C$  denotes a circle of diameter  $d = 1$  with center at  $(x_c, y_c)$ . The boundary and initial conditions are given as:

$$\mathbf{u} = [\gamma(y), 0]^T \text{ on } x = 0, \quad (44a)$$

$$\mathbf{u} = [0, 0]^T \text{ on } y = 0, H, \quad (44b)$$

$$\mathbf{u} = [0, 0]^T \text{ on cylinder } C, \quad (44c)$$

$$\hat{\mathbf{n}} \cdot (-p\mathbf{I} + \nu \nabla \mathbf{u}) = 0 \text{ on } x = L, \quad (44d)$$

where the inlet flow profile  $\gamma(y)$  is given by

$$\gamma(y) = 4u_c y (H - y) / H^2, \quad (45)$$

which is a parabolic profile with  $\gamma(0) = \gamma(H) = 0$  and  $\gamma_m := \gamma(H/2) = u_c$ . The average inlet velocity is given by  $\bar{\gamma} = 2/3u_c$ . The Reynolds number for this problem is defined as  $Re = \frac{U_{ref}d}{\nu}$ .  $U_{ref} = \gamma_m = u_c$ . The force on the cylinder in the direction  $\mathbf{w}$  is expressed as

$$F_w = \int_{\Gamma_C} [(-p\mathbf{I} + \nu [\nabla \mathbf{u} + \nabla \mathbf{u}^T]) \cdot \hat{\mathbf{n}}] \cdot \mathbf{w} \, dS. \quad (46)$$

We set  $\mathbf{w} = (1, 0)$  to extract the drag force, and  $\mathbf{w} = (0, 1)$  to extract the lift force. The drag coefficient  $C_d$  and the lift coefficient  $C_l$  are then calculated as

$$C_d = \frac{2F_{\text{drag}}}{AU^2} = 2F_{\text{drag}}, \quad (47)$$

$$C_l = \frac{2F_{\text{lift}}}{AU^2} = 2F_{\text{lift}} \quad (48)$$

where  $A = 1$  and  $U = 1$  are the reference area and speed respectively.

After a sufficient time is passed, the solution of this example is known to reach either a steady state or a periodic state depending on whether the Reynolds number is below or above a critical value. When the solution achieves a periodic state, so do the drag and lift forces calculated above. Suppose  $T_p$  is the time period of the lift coefficient  $C_l$  obtained from the numerical simulation. Then the corresponding Strouhal number is calculated as

$$St = \frac{L}{UT_p} = \frac{1}{T_p} \quad (49)$$

where  $L = 1$  and  $U = 1$  are the reference length and the speed respectively.

We solve this problem numerically for various Reynolds numbers, and compute the the drag coefficient  $C_d$  and the Strouhal number  $St$  for each case. [Figure 7](#) shows a plot of these  $C_d$  and  $St$  values (along with reference values from the literature). In this example, all the linear methods perform approximately the same.

## 5.4 Turbulent channel flow (3D)

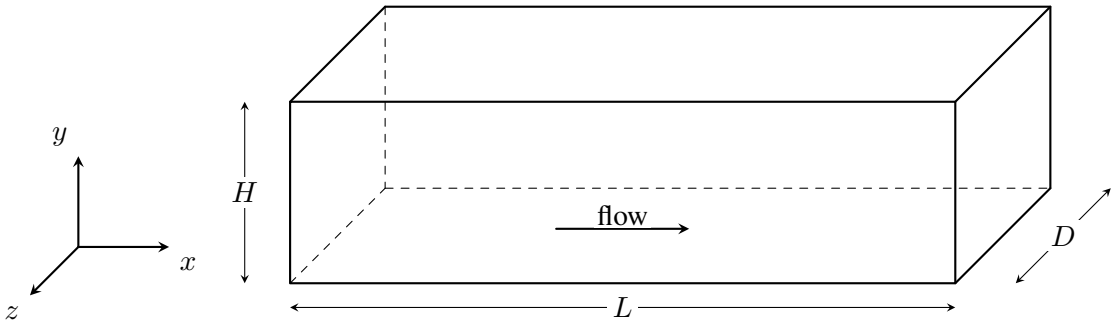


Figure 8: Turbulent channel geometry. Periodic boundary conditions are applied on the streamwise ( $x$ ) and the spanwise ( $z$ ) directions, whereas no-slip conditions are applied on the walls ( $y$ -boundaries).

Starting from this section, we extend our numerical tests to 3D cases. For ease of representation, in this section, we will use  $\mathbf{x} = [x, y, z]^T$  and  $\mathbf{u} = [u_x, u_y, u_z]^T$ . The first test case is a periodic fluid cell sandwiched between two stationary plates and subjected to a unit body force  $\mathbf{f}$  in the streamwise ( $x$ ) direction, forming a ‘3D channel’.

We borrow our problem settings from [2], [33], and [34]. The problem geometry is defined as  $\Omega = I_x \times I_y \times I_z$ , where  $I_x = [0, L]$ ,  $I_y = [0, H]$ , and  $I_z = [0, D]$  as shown in [Figure 8](#). The boundary conditions are

$$\mathbf{u} = \mathbf{0} \text{ on } y = 0, \quad (50a)$$

$$\mathbf{u} = \mathbf{0} \text{ on } y = H, \quad (50b)$$

$$\mathbf{u}(0, y, z, t) = \mathbf{u}(L, y, z, t), \quad (50c)$$

$$\mathbf{u}(x, y, 0, t) = \mathbf{u}(x, y, D, t). \quad (50d)$$

The initial velocity field is constructed using a known mean velocity profile  $U_{\text{mean}}(y)$  obtained from the direct numerical simulation (DNS) database [35]. The mean velocity profile is then linearly interpolated, and a random perturbation field is added. The initial condition is given by,

$$\mathbf{u}(\mathbf{x}, 0) = \begin{bmatrix} U_{\text{mean}}(y) + 0.1 U_{\text{bulk}} \psi(\mathbf{x}) \\ 0.1 U_{\text{bulk}} \psi(\mathbf{x}) \\ 0.1 U_{\text{bulk}} \psi(\mathbf{x}) \end{bmatrix}. \quad (51)$$

Here,  $U_{\text{bulk}}$  denotes the bulk velocity, defined as

$$U_{\text{bulk}} = \frac{1}{H} \int_0^H U_{\text{mean}}(y) dy, \quad (52)$$

while the  $\psi(\mathbf{x}) \in [-1, 1]$  is the perturbation function [2] generated using a C++ pseudo-random number generator. Additionally, we set our forcing function  $\mathbf{f}$  in (1) as  $[1, 0, 0]^T$ . It is important to note that by applying momentum balance in a fully-developed flow, the magnitude of  $\mathbf{f}$  gives an *a priori* estimate of the characteristic (or friction) velocity  $u_\tau$  in our simulation by the relation (53a). However, the effective friction velocity can be computed *a posteriori* from the numerical wall shear stress (53b).

$$u_\tau^{\text{a-priori}} = \sqrt{f_x}, \quad (53a)$$

$$u_\tau^{\text{a-posteriori}} = \sqrt{\nu \left. \frac{\partial u_x}{\partial y} \right|_{y=H}}. \quad (53b)$$

We run our simulations for  $\nu^{-1} = 180, 395$ , and  $590$ . We choose the channel half-width to be the characteristic length  $\delta = H/2$  and set  $\delta$  to 1. The characteristic  $Re_\tau$  and the corresponding geometric and mesh configurations are listed in [Table 3](#). We use a uniform mesh in the streamwise ( $x$ ) and spanwise ( $z$ ) directions and a stretched mesh in the wall-normal direction ( $y$ ), with clustering near the wall. We use  $\Delta t = 10^{-3}$  for all three cases. We introduce the ensemble averaging operator  $\langle \cdot \rangle(y)$  and fluctuation velocity  $u'_x$  in (54). Here, the superscript

Table 3: Grid resolution for turbulent channel flow (3D) simulations

$Re_\tau^{\text{a-priori}}$	$L$	$H$	$D$	Resolution ( $N_x \times N_y \times N_z$ )
180	$2\pi$	2	$(4/3)\pi$	$32 \times 32 \times 32$
395	$2\pi$	2	$\pi$	$64 \times 64 \times 64$
590	$2\pi$	2	$\pi$	$64 \times 64 \times 64$

prime denotes fluctuation and not the fine-scale model velocity mentioned in [Section 2.3](#).

$$\langle u_x \rangle(y) = \frac{1}{T \cdot L \cdot D} \int_{t_{\text{st}}}^T \int_0^L \int_0^D u_x(\mathbf{x}, t) dz dx dt, \quad (54a)$$

$$u'_x(\mathbf{x}, t) = u_x(\mathbf{x}, t) - \langle u_x \rangle, \quad (54b)$$

where  $T$  denotes a large time ( $T - t_{\text{st}} > 100$ ) after the statistical steady state is reached at  $t = t_{\text{st}}$ . We present six turbulent statistics for the largest  $Re_\tau$  ( $= 590$ ) simulated and compare them with the DNS data from [33] shown in [Figure 9](#). Here,  $y^+$  and  $\langle u_x \rangle^+$  denote wall-normal distance and mean streamwise velocity expressed in viscous wall units, following the standard definitions used in [33]. The simulation results for the other two  $Re_\tau$  ( $= 180$  and  $395$ ) are included in the appendix [Section A](#).

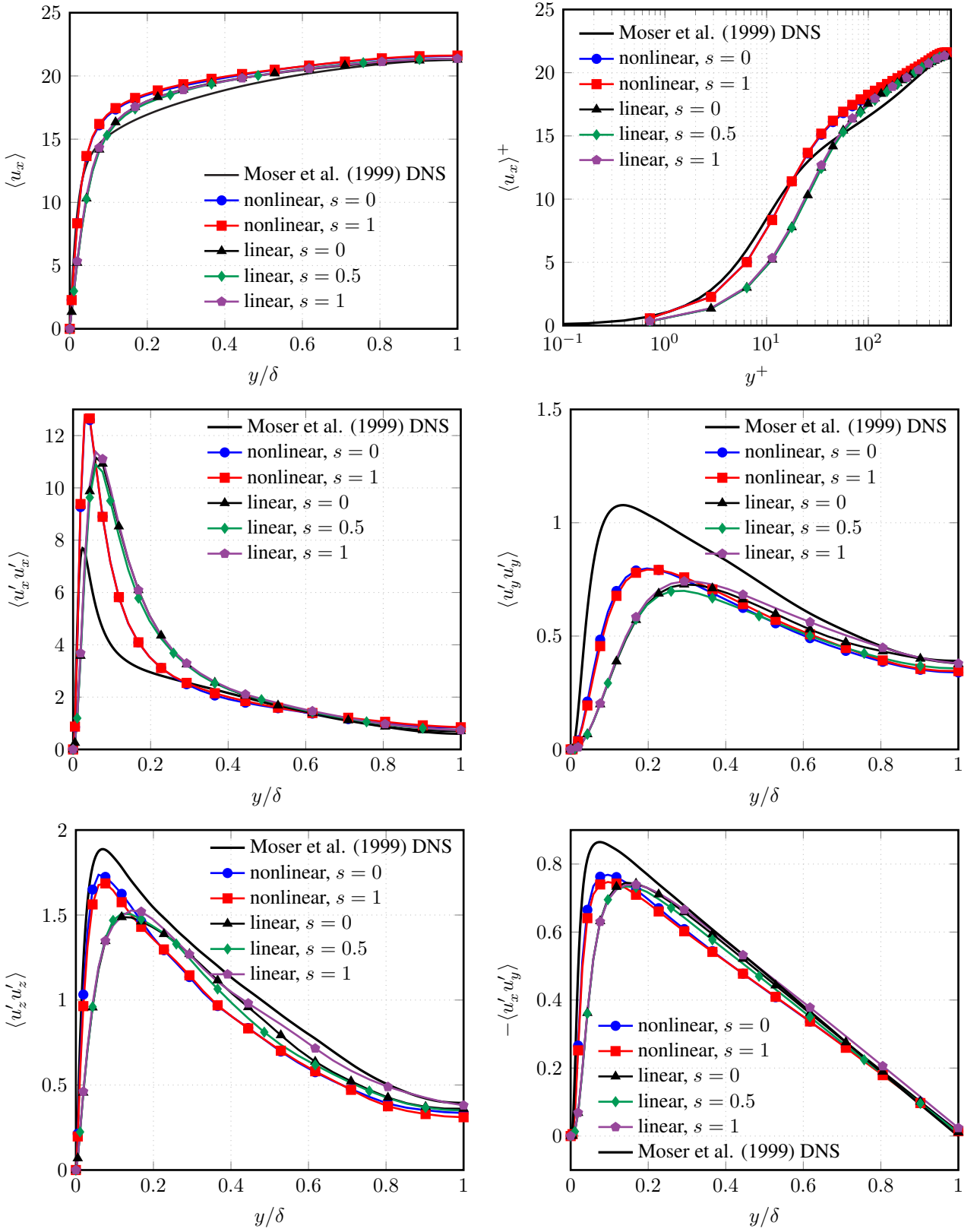


Figure 9: Turbulent statistics for channel flow 3D case at  $Re_\tau = 590$

## 5.5 Flow over an airfoil

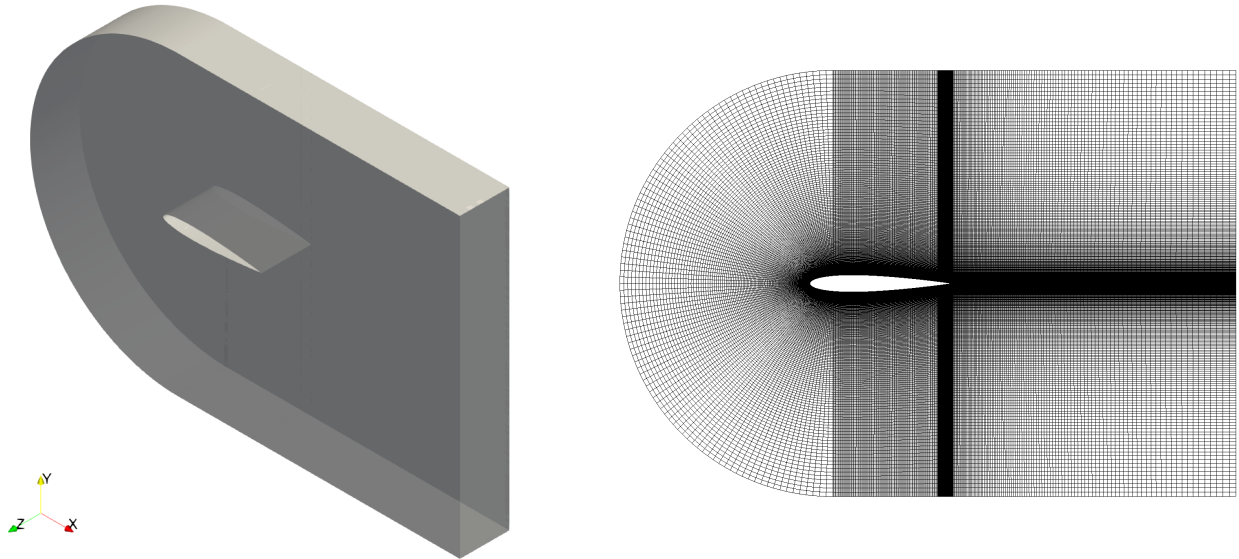


Figure 10: Geometry (left) and mesh (right) for the flow past an airfoil example. Periodic conditions are applied on the spanwise ( $z$ ) directions.

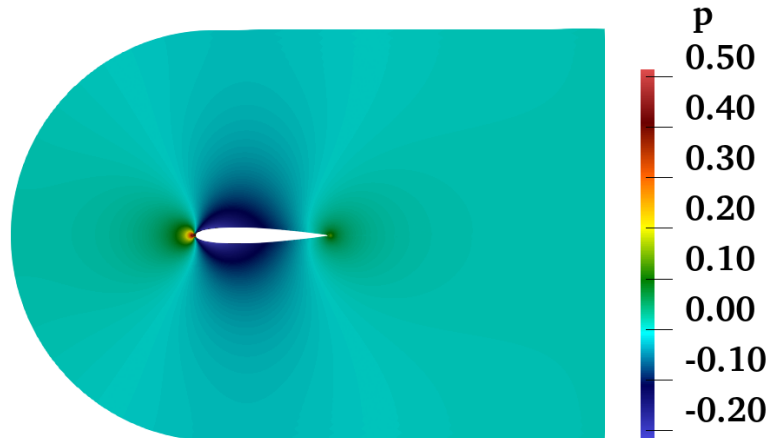


Figure 11: Pressure distribution

Three dimensional turbulent flow over NACA0012 airfoil [36, 37, 38, 39] at chord Reynolds number of 6 million is simulated using this variational multiscale framework we developed for linearized navier stokes equations. The chord length of the airfoil is 1 and angle of attack is 0 degrees. The boundary conditions used for the simulation are as follows: The left, top and bottom wall are prescribed with Dirichlet boundary condition with  $u_x = 1$ ,  $u_y = 0$  and  $u_z = 0$ . The right boundary is prescribed with a traction free boundary condition. The airfoil surface is prescribed with no-slip boundary condition.

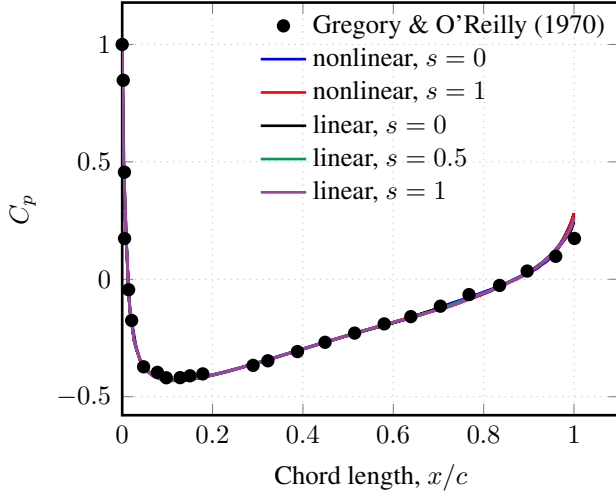


Figure 12: Surface Pressure Coefficient,  $C_p$

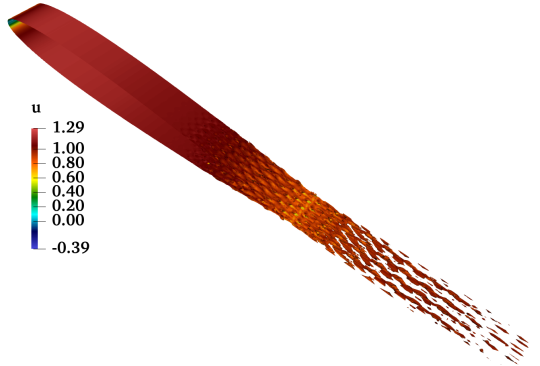


Figure 13: Isosurface of vorticity colored by  $u$

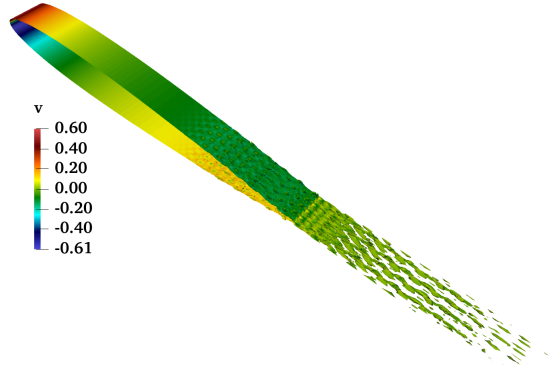


Figure 14: Isosurface of vorticity colored by  $v$

The computational domain shown in Figure 10 extends 1 chord length upstream of the leading edge, 2 chord lengths downstream of the trailing edge and 1.5 chord lengths above and below the airfoil. The mesh consists of approximately 2 million nodes. The surface pressure coefficient ( $C_p$ ) is compared with experimental measurements reported by Gregory and O'Reilly [36]. The pressure coefficient ( $C_p$ ) is calculated using the following equation.

$$C_p = \frac{p - p_\infty}{\frac{1}{2} \rho_\infty u_\infty^2} \quad (55)$$

Here,  $p_\infty$  is the freestream pressure,  $\rho_\infty$  is the freestream density and  $u_\infty$  is the freestream velocity. The free-stream conditions are  $u_\infty = 1$ ,  $\rho_\infty = 1$ , and  $p_\infty = 0$ . Here  $p$  is the mean pressure on the airfoil surface obtained from the simulation. The comparison is shown in Figure 12 and we can see a good agreement between the two results. Additionally, vorticity isosurfaces colored by the velocity components are shown to qualitatively visualize the flow structure around the airfoil in Figure 13 and 14.

## 5.6 Computation time

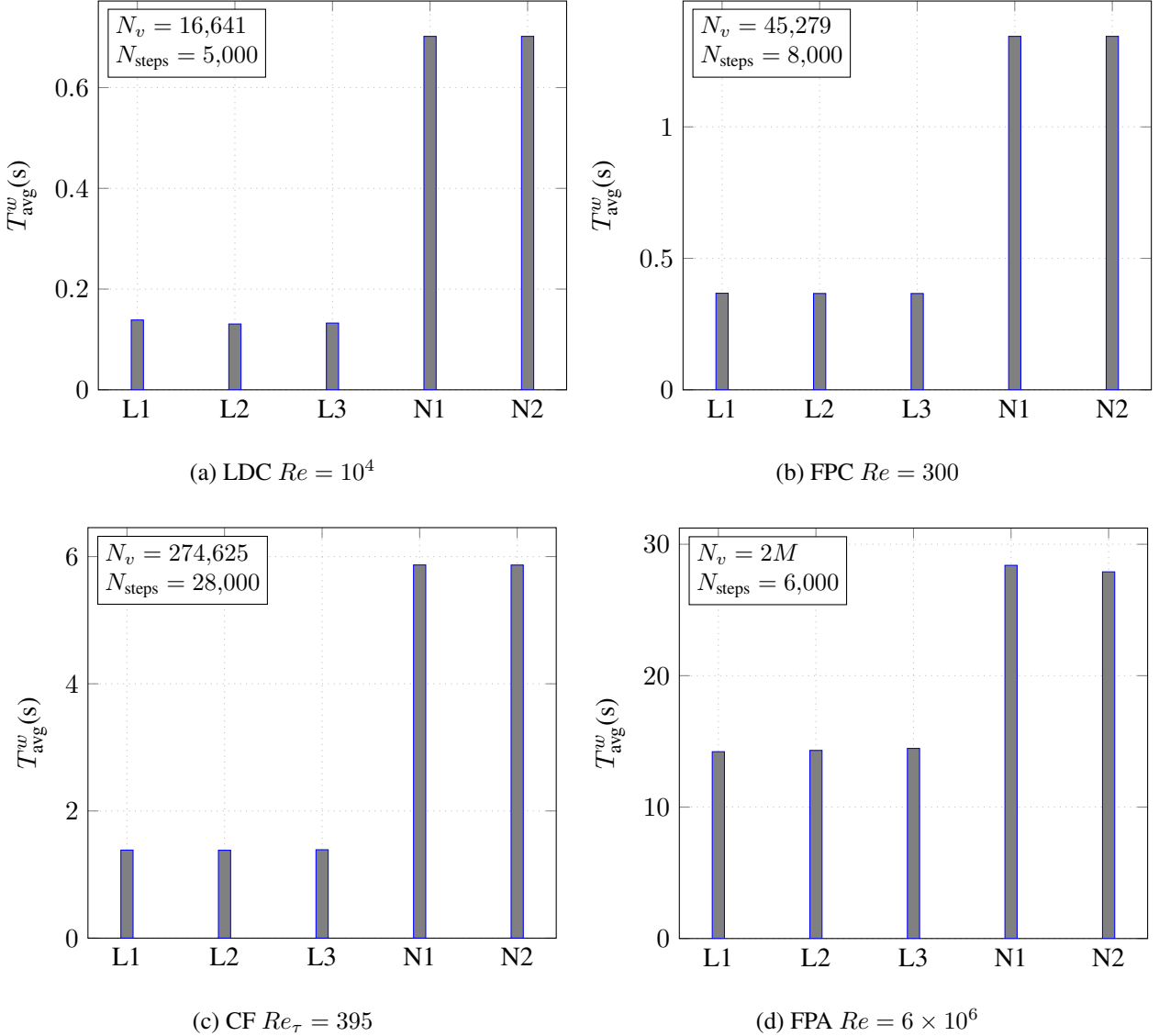


Figure 15: Average time taken (in wall clock time) per time step in the four benchmark cases. Here, L1, L2 and L3 refer to the linear methods with  $s = 0, 1/2$  and 1 respectively. Similarly, N1 and N2 stand for the nonlinear methods with  $s = 0$  and 1 respectively. The number of steps used for calculating the averages are indicated in parenthesis in each subcaption.

In the previous sections, we have established the accuracy and reliability of the proposed semi-implicit method across various standard benchmark problems. Now, in this section, we analyze their performance with respect to the time spent (in wall-clock units) in solving these problems. We collect the total solve time over a set number of time steps, and calculate the average solve time as  $T_{\text{avg}}^w = T_{\text{total}}^w / N_{\text{steps}}$ , where the  $w$  denotes wall-clock time.

In Figure 15, we present a comparison of  $T_{\text{avg}}^w$  for the linear (39) and the nonlinear methods (24). The three linear methods L1, L2 and L3 denote  $s = 0, 1/2, 1$  respectively; and the nonlinear methods N1 and N2 denote  $s = 0, 1$  respectively. For each case, we have included the number of nodes in the mesh (denoted by  $N_v$ ) and the total number of steps ( $N_{\text{steps}}$ ) over which the wall-times are calculated. Within each case, the mesh and all other input data parameters are kept equal across different methods. We can see that the linear methods are roughly 2-4 times faster than the nonlinear methods. This gain is important when we consider the large number time steps involved, especially in 3D problems. For example, if we focus on 15c, the total time taken by the nonlinear methods is roughly 47 hours as opposed to roughly 10 hours by the linear cases. Similarly, in 15d, the total time taken by the nonlinear methods is roughly 47 hours whereas the linear methods take roughly 27

Table 4: Number of Newton iterations (SNES iterations in PETSc) for the 3D cases with nonlinear formulation.

Formulation	$s$	Channel flow			Flow past airfoil $\text{Re}_\tau = 2000$
		$\text{Re}_\tau = 180$	$\text{Re}_\tau = 395$	$\text{Re}_\tau = 590$	
Nonlinear	0	3	3	3	3
Nonlinear	1	3	3	3	3

Table 5: Number of average KSP iterations required per time step for the 3D cases. The specified relative tolerance is set to  $10^{-6}$  in all cases.

Formulation	$s$	Channel flow			Flow past airfoil $\text{Re} = 6M$
		$\text{Re}_\tau = 180$	$\text{Re}_\tau = 395$	$\text{Re}_\tau = 590$	
Linear	0	87.8	190.6	189.8	1126.9
Linear	$\frac{1}{2}$	88.0	191.3	189.5	1130.3
Linear	1	88.1	191.5	190.0	1127.5
Nonlinear	0	293.9	700.7	676.0	2095.7
Nonlinear	1	294.4	702.0	682.3	2062.4

hours.

[Table 4](#) shows that on average, roughly 3 Newton iterations are taken per time step in all the 3D cases (channel flow and airfoil). In [Table 5](#), we present the average number of KSP iterations (i.e., the Krylov subspace iterations) performed per time step. In case of the linear methods, this relates to solving just one linear system, whereas, in case of nonlinear methods, multiple successive linear systems are solved per time step. For the same mesh and parallelization, the time taken by each KSP iteration is roughly same.

## 6 Conclusions

We presented a semi-implicit residual-based variational multiscale (VMS) formulation for the incompressible Navier–Stokes equations. The method linearizes the nonlinear convection contribution by transporting the unknown velocity with an extrapolated convection field. This Oseen-type approximation has a significant structural consequence in the VMS setting: the resulting linear advection operator admits an exact adjoint relation in the weak form, which enables the representation of convection-related fine-scale terms without introducing spatial derivatives of the modeled fine scales. This yields a uniform, implementation-ready stabilized formulation without case-dependent manipulations of the fine-scale derivatives.

The formulation is developed for a generalized linear advection operator  $[(\mathbf{u} \cdot \nabla)\mathbf{u} + s(\nabla \cdot \mathbf{u})\mathbf{u}]$  with  $s \in \{0, \frac{1}{2}, 1\}$ , corresponding to the convective, skew-symmetric, and divergence forms. Across the numerical studies considered, the linear methods with  $s = 0$  and  $s = \frac{1}{2}$  were consistently accurate and robust. The  $s = 1$  linear method performed comparably in settings with outlet and/or periodic boundary conditions, but it was less reliable in problems dominated by Dirichlet boundary conditions, where it did not exhibit the same convergence and robustness under refinement.

A practical advantage of the proposed semi-implicit approach is that each time step requires only a single linear solve. In our benchmarks, this translated to a  $2\text{--}4\times$  reduction in wall-clock time relative to fully implicit nonlinear VMS while maintaining comparable accuracy in the regimes where the method is stable. This speedup is particularly relevant for parameter studies, design and optimization loops, and long-horizon computations that require a rapid approach to steady or statistically steady behavior.

Future work will focus on (i) a more detailed characterization of the boundary-condition sensitivity of the  $s = 1$  linear form and remedies for improved robustness, (ii) extensions to complex-geometry discretizations and immersed-boundary approaches where the derivative-free fine-scale structure is especially advantageous, and (iii) assessing the method in large-scale three-dimensional turbulent simulations where solver scalability and time-to-solution are primary constraints.

## 7 Acknowledgments

This work was partly supported by the National Science Foundation under the grants NSF LEAP-HI 2053760, NSF 1935255.

## References

- [1] Jean Donea and Antonio Huerta. *Finite element methods for flow problems*. John Wiley & Sons, 2003.
- [2] Volker John. *Finite element methods for incompressible flow problems*. Springer, 2016.
- [3] Ivo Babuška. Error-bounds for finite element method. *Numerische Mathematik*, 16(4):322–333, 1971.
- [4] Franco Brezzi. On the existence, uniqueness and approximation of saddle-point problems arising from lagrangian multipliers. *Publications mathématiques et informatique de Rennes*, (S4):1–26, 1974.
- [5] Leopoldo P Franca, G Hauke, and A Masud. Stabilized finite element methods. International Center for Numerical Methods in Engineering (CIMNE), Barcelona . . ., 2004.
- [6] Michel Crouzeix and P-A Raviart. Conforming and nonconforming finite element methods for solving the stationary stokes equations i. *Revue française d'automatique informatique recherche opérationnelle. Mathématique*, 7(R3):33–75, 1973.
- [7] William H Reed and Thomas R Hill. Triangular mesh methods for the neutron transport equation. Technical report, Los Alamos Scientific Lab., N. Mex.(USA), 1973.
- [8] Cedric Taylor and Paul Hood. A numerical solution of the navier-stokes equations using the finite element technique. *Computers & Fluids*, 1(1):73–100, 1973.
- [9] Douglas N Arnold, Franco Brezzi, and Michel Fortin. A stable finite element for the stokes equations. *Calcolo*, 21(4):337–344, 1984.
- [10] Alexander N Brooks and Thomas JR Hughes. Streamline upwind/petrov-galerkin formulations for convection dominated flows with particular emphasis on the incompressible navier-stokes equations. *Computer methods in applied mechanics and engineering*, 32(1-3):199–259, 1982.
- [11] Thomas JR Hughes, Leopoldo P Franca, and Marc Balestra. A new finite element formulation for computational fluid dynamics: V. circumventing the babuška-brezzi condition: A stable petrov-galerkin formulation of the stokes problem accommodating equal-order interpolations. *Computer Methods in Applied Mechanics and Engineering*, 59(1):85–99, 1986.
- [12] Jim Douglas and Jun Ping Wang. An absolutely stabilized finite element method for the stokes problem. *Mathematics of computation*, 52(186):495–508, 1989.
- [13] Tayfun E Tezduyar. Stabilized finite element formulations for incompressible flow computations. *Advances in applied mechanics*, 28:1–44, 1991.
- [14] Thomas JR Hughes. Multiscale phenomena: Green's functions, the dirichlet-to-neumann formulation, subgrid scale models, bubbles and the origins of stabilized methods. *Computer methods in applied mechanics and engineering*, 127(1-4):387–401, 1995.
- [15] Jean-Luc Guermond. Stabilization of galerkin approximations of transport equations by subgrid modeling. *ESAIM: Mathematical Modelling and Numerical Analysis*, 33(6):1293–1316, 1999.
- [16] Thomas JR Hughes, Luca Mazzei, and Kenneth E Jansen. Large eddy simulation and the variational multiscale method. *Computing and visualization in science*, 3(1):47–59, 2000.
- [17] Y Bazilevs, VM Calo, JA Cottrell, TJR Hughes, A Reali, and G Scovazzi. Variational multiscale residual-based turbulence modeling for large eddy simulation of incompressible flows. *Computer methods in applied mechanics and engineering*, 197(1-4):173–201, 2007.

[18] Ivo Babuška. The finite element method with lagrangian multipliers. *Numerische Mathematik*, 20(3):179–192, 1973.

[19] Thomas JR Hughes, Leopoldo P Franca, and Gregory M Hulbert. A new finite element formulation for computational fluid dynamics: Viii. the galerkin/least-squares method for advective-diffusive equations. *Computer methods in applied mechanics and engineering*, 73(2):173–189, 1989.

[20] Ramon Codina. Comparison of some finite element methods for solving the diffusion-convection-reaction equation. *Computer methods in applied mechanics and engineering*, 156(1-4):185–210, 1998.

[21] Tayfun E Tezduyar, Sanjay Mittal, SE Ray, and R Shih. Incompressible flow computations with stabilized bilinear and linear equal-order-interpolation velocity-pressure elements. *Computer Methods in Applied Mechanics and Engineering*, 95(2):221–242, 1992.

[22] Farzin Shakib, Thomas JR Hughes, and Zdeněk Johan. A new finite element formulation for computational fluid dynamics: X. the compressible euler and navier-stokes equations. *Computer Methods in Applied Mechanics and Engineering*, 89(1-3):141–219, 1991.

[23] George Karypis, Kirk Schloegel, and Vipin Kumar. *Parmetis. Parallel graph partitioning and sparse matrix ordering library. Version*, 2, 2003.

[24] Satish Balay, Kris Buschelman, William D Gropp, Dinesh Kaushik, Matthew G Knepley, L Curfman McInnes, Barry F Smith, and Hong Zhang. *Petsc*. See <http://www.mcs.anl.gov/petsc>, 2001.

[25] Hari K Kodali and Baskar Ganapathysubramanian. Computer simulation of heterogeneous polymer photovoltaic devices. *Modelling and Simulation in Materials Science and Engineering*, 20(3):035015, 2012.

[26] Robert Dyja, Baskar Ganapathysubramanian, and Kristoffer G van der Zee. Parallel-in-space-time, adaptive finite element framework for nonlinear parabolic equations. *SIAM Journal on Scientific Computing*, 40(3):C283–C304, 2018.

[27] Biswajit Khara, Robert Dyja, Kumar Saurabh, Anupam Sharma, and Baskar Ganapathysubramanian. Solving fluid flow problems in space-time with multiscale stabilization: formulation and examples. *arXiv preprint arXiv:2402.12571*, 2024.

[28] UKNG Ghia, Kirti N Ghia, and CT Shin. High-re solutions for incompressible flow using the navier-stokes equations and a multigrid method. *Journal of computational physics*, 48(3):387–411, 1982.

[29] Sintu Singha and KP Sinhamahapatra. Flow past a circular cylinder between parallel walls at low reynolds numbers. *Ocean Engineering*, 37(8-9):757–769, 2010.

[30] Luigino Zovatto and Gianni Pedrizzetti. Flow about a circular cylinder between parallel walls. *Journal of Fluid Mechanics*, 440:1–25, 2001.

[31] Nicolas Kanaris, Dimokratis Grigoriadis, and Stavros Kassinos. Three dimensional flow around a circular cylinder confined in a plane channel. *Physics of fluids*, 23(6), 2011.

[32] Michael Schäfer, Stefan Turek, Franz Durst, Egon Krause, and Rolf Rannacher. *Benchmark computations of laminar flow around a cylinder*. Springer, 1996.

[33] Robert D Moser, John Kim, Nagi N Mansour, et al. Direct numerical simulation of turbulent channel flow up to  $re= 590$ . *Phys. fluids*, 11(4):943–945, 1999.

[34] Volker Gravemeier. Scale-separating operators for variational multiscale large eddy simulation of turbulent flows. *Journal of Computational Physics*, 212(2):400–435, 2006.

[35] Robert D Moser, John Kim, and Nagi N Mansour. Database of direct numerical simulation of 3d turbulent channel flow. <https://turbulence.oden.utexas.edu/data/MKM/>, 1999. Accessed: 2025-09-15.

[36] N. Gregory and C. L. O'Reilly. Low-speed aerodynamic characteristics of naca 0012 aerofoil sections, including the effects of upper-surface roughness simulation hoar frost. Reports and Memoranda 3726, National Physical Laboratory, Teddington, UK, 1970.

[37] W. J. McCroskey. A critical assessment of wind tunnel results for the naca 0012 airfoil. NASA Technical Memorandum NASA-TM-100019, NASA Ames Research Center, Moffett Field, CA, United States, 1987.

[38] C. L. Ladson. Effects of independent variation of mach and reynolds numbers on the low-speed aerodynamic characteristics of the naca 0012 airfoil section. NASA Technical Memorandum NASA-TM-4074, NASA Langley Research Center, Hampton, VA, United States, 1988.

[39] Seyed Mohammad Hosseini, Ricardo Vinuesa, Philipp Schlatter, Ardesir Hanifi, and Dan S Henningson. Direct numerical simulation of the flow around a wing section at moderate reynolds number. *International Journal of Heat and Fluid Flow*, 61:117–128, 2016.

## A Additional results on channel flow (3D)

**Case 1: Reynolds number  $Re_\tau = 180$**

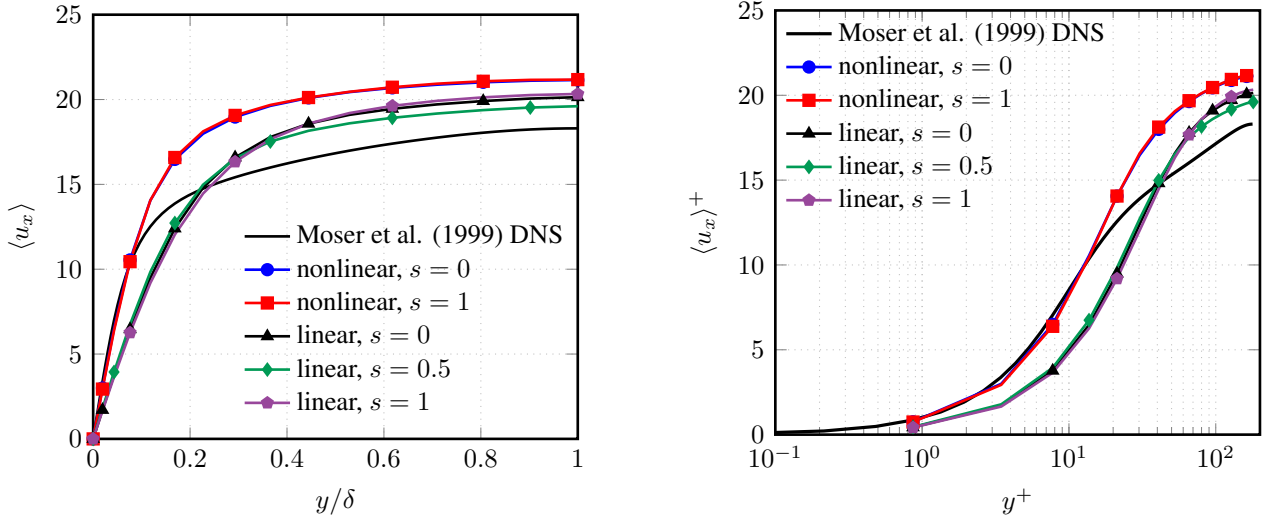


Figure 16: The mean velocity profile for  $Re_\tau = 180$

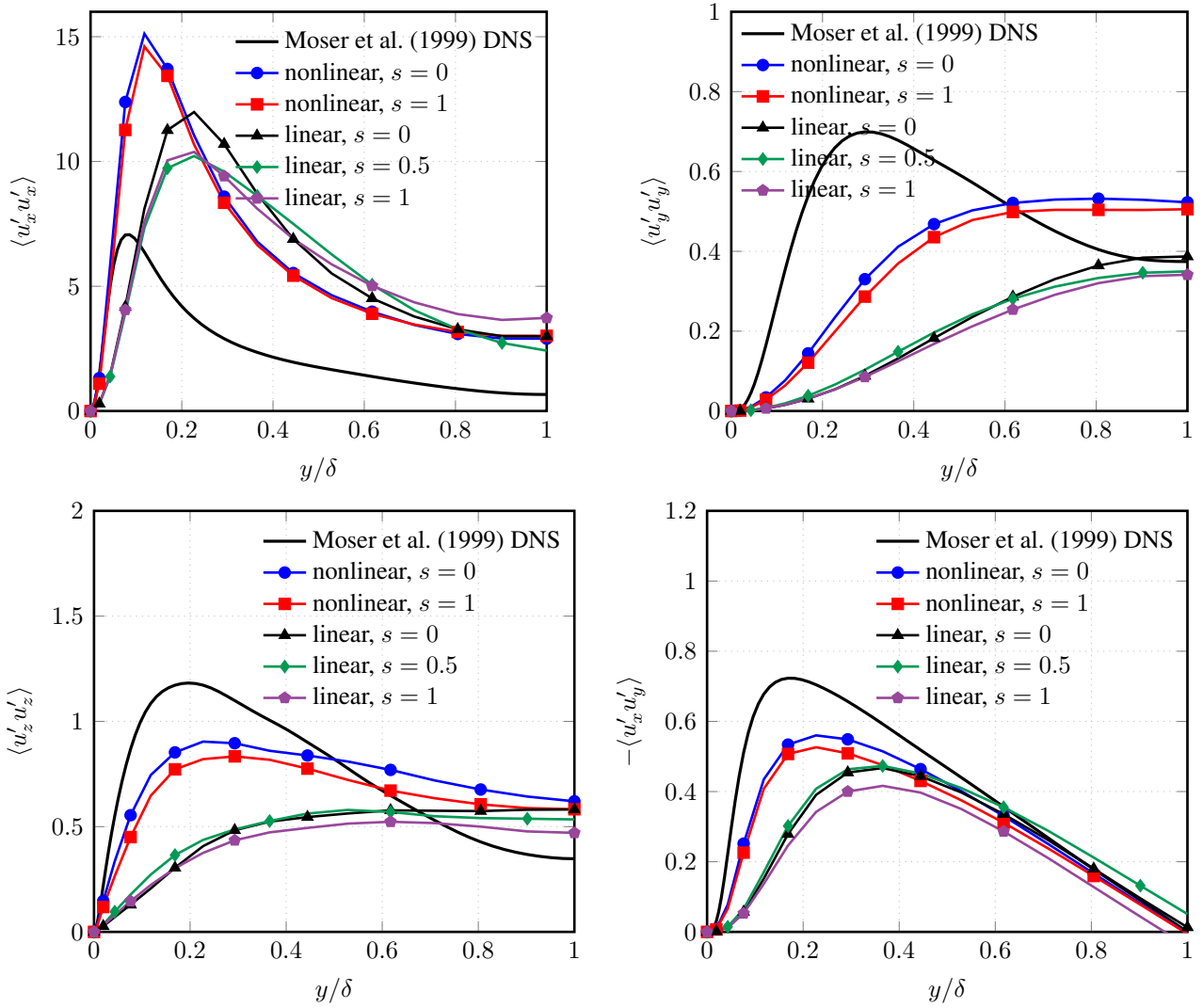


Figure 17: Reynolds stress for  $Re_\tau = 180$

**Case 2: Reynolds number  $Re_\tau = 395$**

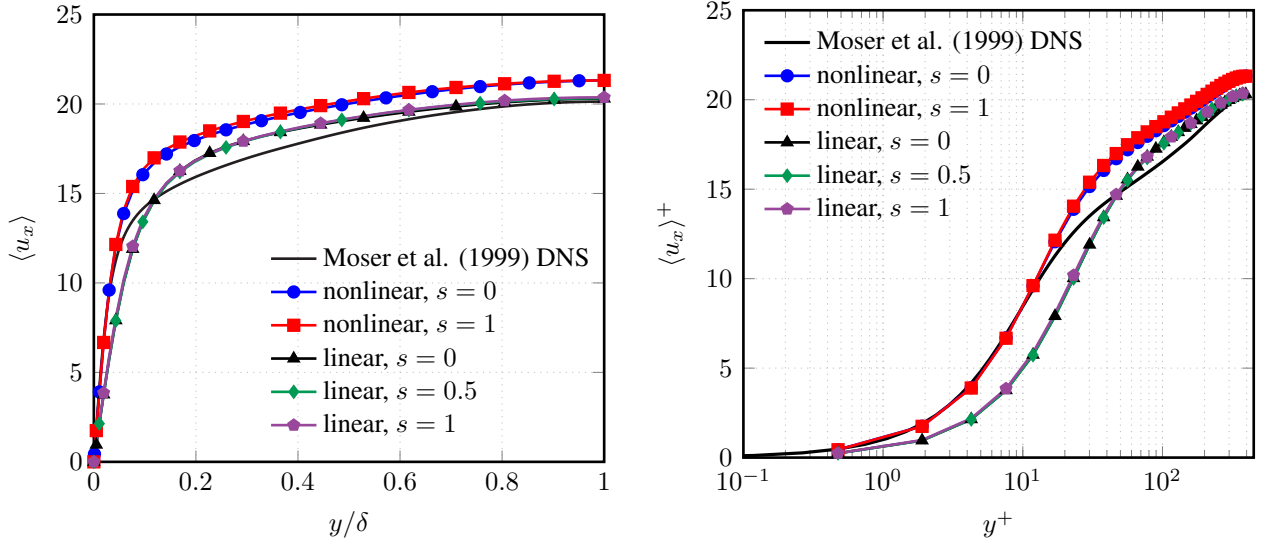


Figure 18: The mean velocity profile for  $Re_\tau = 395$

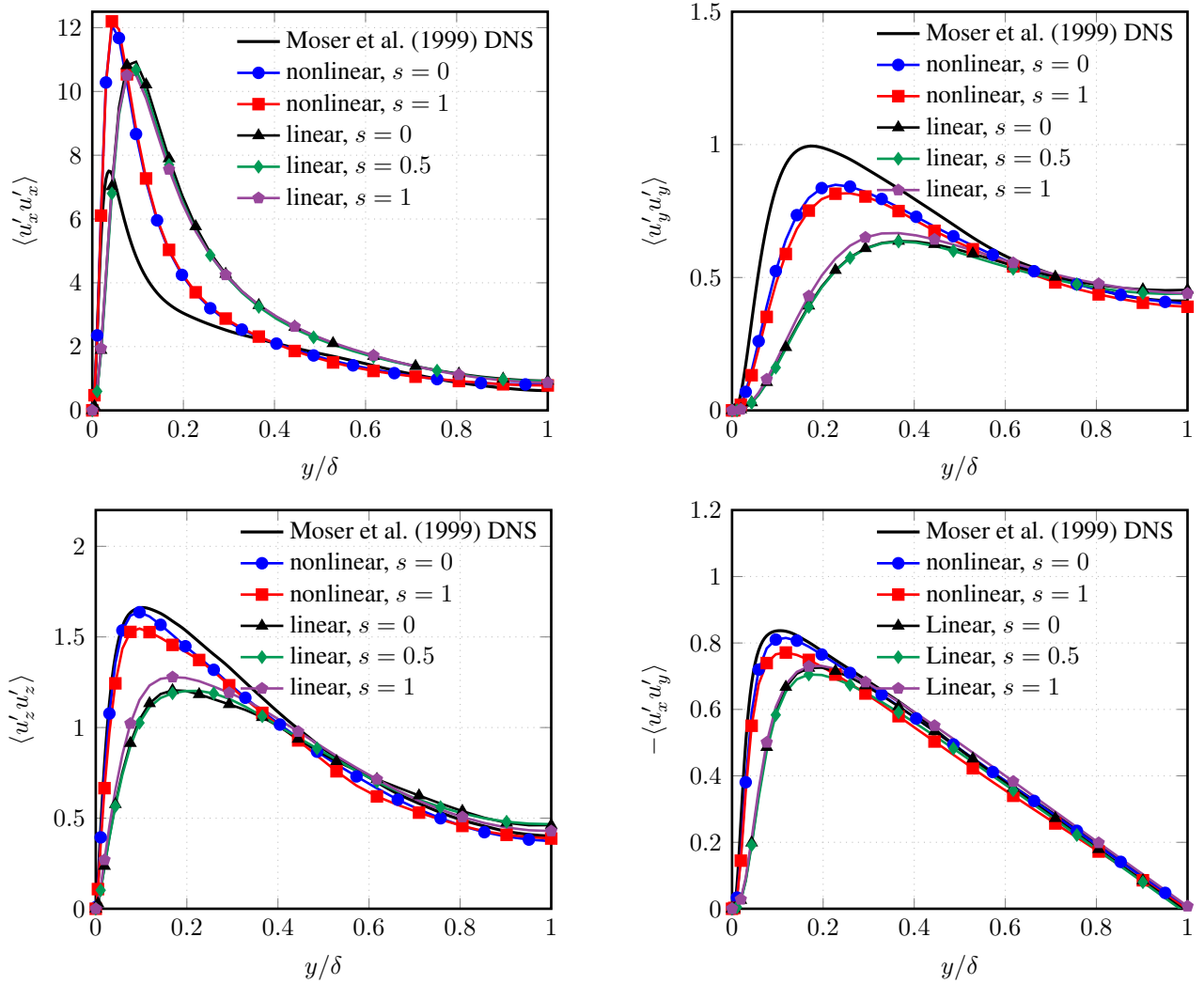


Figure 19: Reynolds stress for  $Re_\tau = 395$